



Interfacial confinement effect induced by pre-sulfurization for promoting SO₂ tolerance of MnFe-TOS catalyst in low temperature NH₃-SCR reaction

Xiaosheng Huang ^{a,c,1}, Ningjie Fang ^{b,1}, Shilin Wu ^b, Fang Dong ^a, Yinghao Chu ^b, Zhicheng Tang ^{a,c,*}

^a National Engineering Research Center for Fine Petrochemical Intermediates, State Key Laboratory for Oxo Synthesis and Selective Oxidation, Lanzhou Institute of Chemical Physics, Chinese Academy of Sciences, Lanzhou 730000, China

^b College of Architecture and Environment, Sichuan University, Chengdu 610000, China

^c Shandong Laboratory of Advanced Materials and Green Manufacturing at Yantai, Yantai Zhongke Research Institute of Advanced Materials and Green Chemical Engineering, Yantai 264006, China



ARTICLE INFO

Keywords:

Pre-sulfurization
Interfacial confinement effect
Functional protective site
NH₃-SCR

ABSTRACT

SO₂ poisoning still is an unresolved problem for NH₃-SCR catalysts, especially under low temperature conditions. Herein, a two-pronged approach has been applied on MnFe-TOS for promoting SO₂ tolerance at low temperature in NH₃-SCR process. Pre-sulfurization via inserting SO₄²⁻ into TiO₂ lattice perturbed the local electronic environment to supplement rich surface acid sites, promoting the rapid adsorption of NH₃ at reaction temperature. Active -NH₂ and NH₄⁺ could be quickly consumed by NO/nitrates via both L-H and E-R reaction pathway and resulted in high N₂ selectivity. The strong interaction of Mn-O-Fe induced by interfacial confinement effect regulated redox ability and inhibited the adsorption/oxidation of SO₂, which was benefited to NO activation on MnFe-TOS. At the same time, the (NH₄)₂SO₄ generated during the NH₃-SCR process was prone to dissociation into NH₄⁺ and SO₄²⁻, where NH₄⁺ continued to participate in the SCR reaction, while SO₄²⁻ bonded to Fe, as a functional protective site, allowing the Mn site to be protected. DFT calculations have provided convincing evidence at the molecular level to demonstrate how pre-sulfurization induced lattice distortion and affected chemical adsorption characteristics of catalytic active centers (Mn-O-Fe-S). Consequently, the MnFe-TOS exhibited excellent resistance to SO₂ at low temperature, and the N₂ selectivity has been improved during a wide temperature window. This study provides a new approach for designing efficient and stable NH₃-SCR catalysts.

1. Introduction

As a typical gaseous air pollutant, nitrogen oxide NO_x originated from the use of fossil fuels is an important precursor of PM_{2.5} and threatening human health [1]. A proven technology that selective catalytic reduction of NO_x with NH₃ has been widely applied in industrial flue gas purification [2,3]. Commercial catalysts V₂O₅-WO₃(MoO₃)/TiO₂ are generally accepted in thermal power stations because of good catalytic performance and SO₂/H₂O resistance in high temperature 300–420 °C [4,5]. However, NO_x elimination in the non-electric sector remains daunting challenges due to the catalysts poor activity and resistance to H₂O and SO₂ at low operating temperature (below 300 °C)

[6,7]. In addition, vanadium is bio-toxic and the obsolete spent catalyst will cause secondary pollution to the environment [8,9]. Therefore, it is very urgent to develop environmentally friendly NH₃-SCR catalysts with splendid low-temperature activity and good SO₂/H₂O tolerance to accelerate the process of NO_x elimination in non-electric industries.

Mn-based catalysts are considered as the most promising catalysts for low-temperature denitrification because its variable valence states endowed Mn excellent redox ability at low temperature [10]. However, Mn-based catalysts are sensitive to water vapor and SO₂, where SO₂ can easily oxidize into SO₃ and attack Mn sites to form metal sulfate, resulting in poisoned and deactivated under complex flue gas conditions [11]. Another obstacle that restricts the application of Mn-based

* Corresponding author at: National Engineering Research Center for Fine Petrochemical Intermediates, State Key Laboratory for Oxo Synthesis and Selective Oxidation, Lanzhou Institute of Chemical Physics, Chinese Academy of Sciences, Lanzhou 730000, China.

E-mail address: tangzhicheng@licp.ac.cn (Z. Tang).

¹ Xiaosheng Huang and Ningjie Fang contributed equally to this work.

catalysts is the poor N₂ selectivity mainly caused by N₂O formation [12]. Fe is another inexpensive transition metal element next to Mn, but its catalytic performance in the NH₃-SCR reaction is quite different from that of Mn. Fe-based catalysts mainly exhibit good catalytic activity at medium-high temperature and strong sulfur resistance [13]. It can be seen that the construction of MnFe bimetallic oxide catalysts is expected to enhance the sulfur resistance while widening the low-temperature activity window [14]. Shi et al. found that valence electrons between Fe and Mn redistributed due to the different electronegativity, and different amounts of Mn and Fe led to different electron transport. Thus, the redox ability and acidity of Mn–Fe–BTC could be controlled by varying the content of Mn and Fe [15]. Rare earth modification for improving NH₃-SCR performance also is a research hotspot [16]. Shi et al. prepared Dy-doped MnFe oxides by electrospinning method, and they found that Dy-doping caused the electron density of the predominantly O atoms on the surface of MnFeDy to be more depleted than in the case of MnFe, thus energetically favoring the NH₃ adsorption and NO activation [17]. In addition, designing some special structures of catalysts is also an effective way to improve their catalytic performance. Guo et al. constructed core-shell MnFeO_x @TiO₂ catalyst which possessed more chemisorbed oxygen species, and the TiO₂ shell can also protect active species from poisoning [18]. In our previous work, MnFe@CeO_x core-shell nanocage were employed as a model for investigation, where the CeO₂ shell induced a unique interfacial diffusion effect and improved its NH₃-SCR catalytic performance [19,20].

Despite the variety of MnFe bimetallic oxide catalysts available, the problems of Mn-based catalyst severe SO₂ poisoning and N₂O generation remain unresolved. Generally speaking, the causes of SO₂ poisoning can be summarized as both active site sulfation and ammonium sulfate deposition [6]. Based on this, the effect of sulfation treatment on catalytic activity and appropriate strategies to accelerate the decomposition of ammonium sulfate have been investigated. Xie et al. controlled the amount of sulfate on CeO₂ by varying sulfation time in SO₂ + O₂. They found that more surface sulfate could not only produce more Brønsted acid sites, but also impede the formation of reactive oxygen, thereby increasing the N₂ selectivity [21]. Li et al. explored the contradictory impact of sulfation on NH₃-SCR catalyst, they found that sulfation suppressed the reducibility and O storage ability and reduced the surface-active sites content. At the same time, sulfation could also generate new Brønsted acid sites [22]. Chen et al. reported that the formation mechanism of N₂O on MnFeO_x catalyst mainly followed the NSCR pathway below 150 °C and then turned into over oxidation of NH₃ with increasing temperature [23]. Although tremendous efforts have been made to improve Mn-based catalysts' sulfur resistance and N₂ selectivity, the development of efficient and stable manganese-based catalysts that can be applied to practical scenarios still needs further exploration.

Herein, MnFe-TOS catalyst for NH₃-SCR has been prepared by a simple one-pot hydrothermal method. The skillfully use of TiOSO₄ hydrolysis directly completed the pre-sulfurization in the catalyst synthesis process. Surprisingly, a novel phenomenon of suppressing the formation of N₂O and enhancing SO₂ resistance was found on the MnFe-TOS catalyst. In comparison with ordinary MnFe-TiO₂ catalyst, the redox capacity of MnFe-TOS was weakened by eliminating isolated active Mn sites. Compensate for this, a large number of defects and surface acid sites were supplied due to the perturbation of local electron density by SO₄²⁻ as well as strong interaction between Mn–O–Fe. With the dual impact of pre-sulfurization and interfacial confinement effect, the adsorption and oxidation of SO₂ on catalyst and the generation of N₂O during the SCR process were effectively suppressed. Through comprehensive in situ DRIFTS analysis and DFT calculations, corresponding NH₃-SCR reaction mechanism and stability enhancement effect were revealed in depth.

2. Materials and methods

2.1. Preparation and characterization of catalysts

A facial one-pot hydrothermal method was used to prepare MnFe-TiO_x catalysts. In details, 1 mmol MnSO₄•H₂O, 1 mmol KMnO₄, 4 mmol Fe(NO₃)₃•9 H₂O and 2 g TiOSO₄ were dissolved in 100 mL deionized water with successive stirring. 0.15 g NH₄F and 0.42 g urea dissolved in 40 mL deionized water was dripped slowly into above solution. After that, transferred above solution into a Teflon-lined autoclave heated at 120 °C for 16 h. Allow to cool to room temperature, washing the precipitate with deionized water 6 times by centrifugation. Finally, drying the solid at 80 °C overnight and calcining at 450 °C for 3 h (1 °C/min) in muffle furnace, the obtained catalyst was marked as MnFe-TOS. For comparation, Mn-TOS and Fe-TOS were prepared via the same synthesis method with only equal amounts of MnSO₄/KMnO₄ or Fe(NO₃)₃. In addition, MnFe-TiO₂ was also prepared by replacing TiOSO₄ with industrial titanium dioxide.

Physical and chemical properties of catalysts such as phase composition, microscopic morphology, surface chemical environment, and pore size characters were evaluated via powder X-ray diffraction patterns (XRD), Raman Spectroscopy, TEM, XPS, ICP-OES, and N₂ adsorption experiments. The amount of sulfur deposited on the SO₂-poisoned catalysts was measured via thermal analysis (TG-DSC). The details of NH₃-TPD/SO₂-TPD/O₂-TPD as well as in situ DRIFTS were stated in the [Supporting Information](#).

2.2. Activity measurement

All catalysts NH₃-SCR activities were performed on the fixed-bed reactor (KLYT5010TCP). During the test, 500 ppm NO, 500 ppm NH₃, and 5 vol% O₂ were introduced with N₂ as balanced gas. The total gas flow was controlled 200 mL/min (GHSV = 30,000 h⁻¹), 5 vol% moisture (by injection pump) or/and 150 ppm SO₂ was introduced if needed. The flue gas analyzer (KANE9506) and G200 N₂O analyzer (Geotech) were used to analyze outlet gas concentration, catalytic performance was evaluated by NO conversion ([Eq. 1](#)), and N₂ selectivity was also calculated ([Eq. 2](#)):

$$\text{NO conversion}(\%) = \frac{[\text{NO}]_{\text{in}} - [\text{NO}]_{\text{out}}}{[\text{NO}]_{\text{in}}} \times 100\% \quad (1)$$

$$\text{N}_2 \text{ selectivity}(\%) = \left(1 - \frac{2 \times [\text{N}_2\text{O}]_{\text{out}}}{[\text{NO}]_{\text{in}} - [\text{NO}]_{\text{out}} - [\text{NO}_2]_{\text{out}}} \right) \times 100\% \quad (2)$$

Kinetic analysis methods and DFT calculation details were presented in [supporting information](#).

3. Results and discussions

3.1. Catalytic performance and SO₂ resistance

The NH₃-SCR performance including NO conversion, N₂ selectivity, and tolerance to SO₂/H₂O on as-prepared catalysts were all explored. As shown in [Fig. 1A](#) and D, the MnFe-TiO₂ catalyst showed high catalytic activity below 200 °C, but the N₂ selectivity dropped sharply above 200 °C and even below 10% at 300 °C. Notably, MnFe-TOS exhibited a wider operating temperature window, the NO conversion could reach more than 80% at 180–380 °C, and the N₂ selectivity has been maintained over 90% during the whole temperature range. As for the Mn-TOS, the NO conversion could not reach to 90% until 260 °C, this catalytic activity was much worse than that of Mn-based catalysts reported in other literatures [1,4]. Interestingly, the N₂ selectivity first decreased at 260–340 °C and then gradually recovered at higher temperature. Herein, the limited low-temperature catalytic activity and improved N₂ selectivity may be related to the modification of the catalyst's oxidation-reduction ability by pre sulfurization. Comparably, the

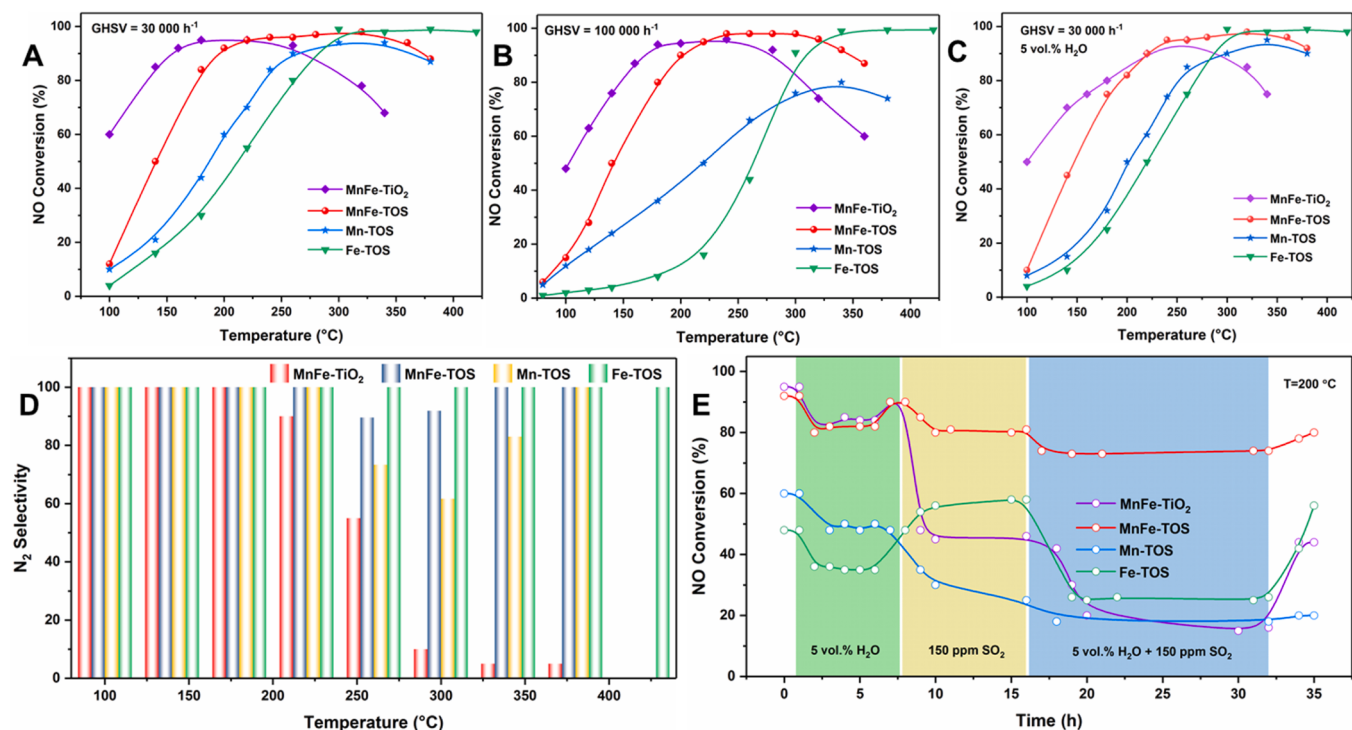


Fig. 1. Catalytic performance evaluation results: NO conversion at (A) GHSV = 30,000 h⁻¹, (B) GHSV = 100,000 h⁻¹, (C) GHSV = 30,000 h⁻¹ containing 5 vol% H₂O, (D) N₂ selectivity, and (E) stability test containing 5 vol% H₂O or/and 150 ppm SO₂.

Fe-TOS exhibited good high-temperature activity, both of the NO conversion as well as the N₂ selectivity were close to 100% upon 300 °C and it showed good thermal stability. The cyclic test results in Fig. S1 indicated that the catalytic activity of each catalyst has good repeatability and testing stability. Besides, the effect of gaseous hourly space velocity on catalytic performance has also been investigated by increasing GHSV to 100,000 h⁻¹. As illustrated in Fig. 1B, despite the Mn-TOS showed inferior catalytic activity, the catalytic performance of other catalysts was less affected. The above experimental phenomenon indicated that although the low-temperature activity of MnFe-TOS, Mn-TOS, and Fe-TOS prepared by hydrolysis of TiOSO₄ were somewhat inhibited, it effectively widened the operating temperature window and significantly improved N₂ selectivity, which might be related to the residual sulfate ions in catalysts.

Tolerance to H₂O/SO₂ for all catalysts were evaluated considering the inevitable presence of water vapor and SO₂ in actual industrial flue gas [24]. As depicted in Fig. 1C and E, the catalytic activity of the MnFe-TiO₂ was significantly suppressed by water vapor at low temperatures, but the NO conversion on the MnFe-TOS still maintained above 80% at 200 °C. When 150 ppm SO₂ was introduced at 200 °C, the catalytic activity of MnFe-TiO₂ was severely inhibited and the NO conversion decreased from 90% to 45%. However, this inhibition was relatively mild on MnFe-TOS, and the NO conversion dropped from 90% to 80%. Interestingly, the Fe-TOS catalyst exhibited a unique SO₂-promoting effect with NO conversion increased from 48% to 58%. Subsequently, 5 vol% H₂O and 150 ppm SO₂ were introduced together, the catalytic activities of Fe-TOS, Mn-TOS, and MnFe-TiO₂ were further inhibited and the NO conversion on the MnFe-TiO₂ sharply dropped to below 20%. Impressively, the inhibitory effect on the MnFe-TOS catalyst was extremely weak, where the NO conversion was still able to be maintained over 74%. Therefore, we concluded that the MnFe-TOS catalyst possessed superior SO₂ tolerance compared to traditional MnFe-TiO₂ catalyst. Below, we will discuss the above experimental phenomenon and conduct an in-depth analysis of the physicochemical properties of the catalysts as well as the mechanism for improving N₂ selectivity and tolerance to SO₂ poisoning.

3.2. Kinetics analysis

For kinetics analysis, the NO conversion was controlled < 20% by using 200 mg catalyst in a fixed-bed for eliminating thermal and diffusion effects at different temperatures [8]. Firstly, turnover frequency (TOF) has been calculated according to literatures report to evaluate the intrinsic activity of catalysts [25]. As shown in Fig. 2A and B, regardless of whether Fe or Mn was used as the active site, the TOF of MnFe-TiO₂ catalyst was always slightly higher than that of MnFe-TOS catalyst, and both of them were significantly higher than those of Mn-TOS and Fe-TOS. This phenomenon indicated that the coexistence of Mn and Fe was beneficial to increase catalysts intrinsic activity, while the pre-sulfurization has a slight inhibitory effect on the catalytic activity. Furthermore, the reaction rates and apparent activation energies have also been investigated [26], and corresponding results were listed in Table 1. A linear relationship between -lnk and 1000/T was well established and the activation energy (E_a) was obtained. As drawn in Fig. 2C, the E_a of MnFe-TOS catalyst for the NO reduction was 24.92 kJ mol⁻¹, which was lower than both of Mn-TOS and Fe-TOS. This indicated that the strong interaction of Mn—O—Fe reduced the catalyst reaction activation energy. However, the E_a of the MnFe-TiO₂ catalyst (19.91 kJ mol⁻¹) was even lower than that of MnFe-TOS, this suggested that the SCR reaction under ideal conditions required less energy at MnFe-TiO₂ catalyst and therefore NO was more easily reduced at lower temperatures. More intuitively, the reaction rate of each catalyst at different temperature was drawn in Fig. 2D. It could be clearly observed that the MnFe-TiO₂ catalyst exhibited the highest reaction rate, followed by the order that MnFe-TOS > Mn-TOS > Fe-TOS. Though the MnFe-TiO₂ catalyst showed better catalytic activity at low temperature, its poor N₂ selectivity and tolerance to SO₂ at high temperature seriously restricted its development and application. In contrast, the catalyst MnFe-TOS exhibited good N₂ selectivity and resistance to SO₂ poisoning while having a wider operating temperature window, making it more valuable for research and application prospects.

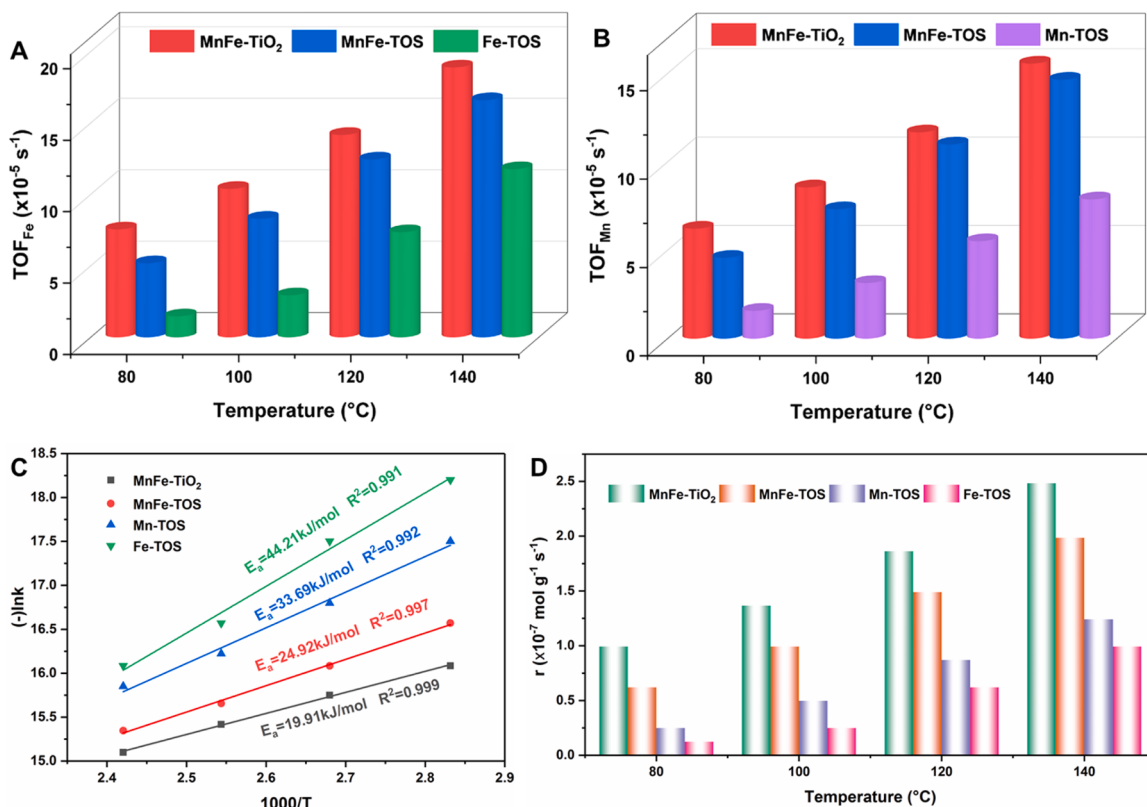


Fig. 2. Kinetic calculation results of (A) TOF_{Fe} , (B) TOF_{Mn} , (C) Arrhenius plots, and (D) reaction rates of each catalyst.

Table 1

Kinetic calculation results of each catalyst.

Catalysts	$k (\times 10^{-7})$				$r (\times 10^{-7} \text{ mol s}^{-1} \text{g}^{-1})$				$E_a (\text{kJ mol}^{-1})$	R^2
	80 $^{\circ}\text{C}$	100 $^{\circ}\text{C}$	120 $^{\circ}\text{C}$	140 $^{\circ}\text{C}$	80 $^{\circ}\text{C}$	100 $^{\circ}\text{C}$	120 $^{\circ}\text{C}$	140 $^{\circ}\text{C}$		
MnFe-TiO ₂	1.03	1.45	2.02	2.77	0.99	1.36	1.86	2.48	19.91	0.999
MnFe-TOS	0.64	1.03	1.59	2.16	0.62	0.99	1.49	1.99	24.92	0.997
Mn-TOS	0.25	0.51	0.90	1.31	0.25	0.50	0.87	1.24	33.69	0.992
Fe-TOS	0.12	0.25	0.64	1.03	0.12	0.25	0.62	0.99	44.21	0.991

3.3. Phase composition and structure analysis

All as-prepared catalysts were detected by XRD patterns to confirm their compositions. As illustrated in Fig. 3A, diffraction peaks on the Fe-TOS patterns appeared at 25.3°, 37.8°, and 48.0° were well indexed to the anatase TiO₂ (JCPDS 84–1285), no other impurity peaks about iron oxides was detected, implying that iron species were in amorphous or highly dispersed. In addition to the anatase diffraction peaks were detected, a series of characteristic peaks of MnO₂ (JCPDS 72–1982) could be observed on the Mn-TOS patterns at 12.7°, 18.1°, 28.7°, and 37.6°, implying that manganese oxides tended to crystallize in the TiO₂ carrier. As for the MnFe-TOS, only anatase TiO₂ characteristic peaks could be observed while both Mn and Fe species were highly dispersed, indicating that synergistic effect between Fe and Mn could inhibit the crystallization of manganese oxides. On the contrary, the MnFe-TiO₂ catalyst not only possessed stronger anatase diffraction peaks, but also clearly exposed the crystalline phase of Mn₂O₃ (JCPDS 76–0150). This phenomenon confirmed the fact that a large number of isolated Mn sites existed on the MnFe-TiO₂ catalyst, which could be easily attacked by SO₂ during the NH₃-SCR process. In addition, the intensity of the diffraction peaks differed significantly from MnFe-TiO₂ to MnFe-TOS, and the crystal size has been calculated by the FWHM of (101) diffraction peak and listed in Table 2, where the TiO₂ grain size obtained by

hydrolysis of TiOSO₄ (9.0 nm) was much smaller than that of commercial TiO₂ (19.0 nm). What's more, a significant peak shift was observed on the (101) plane of MnFe-TOS compared to the MnFe-TiO₂ in partial enlarged drawing of Fig. 3A1. Considering that both Mn and Fe in MnFe-TOS and MnFe-TiO₂ were all introduced via one-pot preparation process, above peak shift phenomenon should be contributed to strong interaction between Mn–O–Fe occurred on the MnFe-TOS catalyst. Since the only difference between MnFe-TOS and MnFe-TiO₂ is the use of different titanium supports, so the SO₄²⁻ generated by the hydrolysis of TiOSO₄ could cause lattice distortion of TiO₂, which may also be another reason for peak shift in XRD.

As a complement to the analysis of the catalyst structure, the Raman spectra was collected in Fig. 3B, where the Raman shifts at 149 cm⁻¹ (E_g), 395 cm⁻¹ (B_{1g}), 510 cm⁻¹ (A_{1g}), and 635 cm⁻¹ (E_g) were all attributed to anatase TiO₂ [8]. Compared with MnFe-TiO₂ catalyst, the highest Raman scattering peak of MnFe-TOS catalyst was significantly blue-shifted 10 cm⁻¹ in partial enlarged drawing of Fig. 3B1, which was well consistent with the XRD results and indicated that the lattice distortion of TiO₂ in the MnFe-TOS occurred, leading to the formation of more surface lattice defects in the anatase phase. Similar phenomenon could also be observed in XPS spectra of Ti2p in Fig. 3D, where 0.2 eV chemical shift to low binding energy was detected on the MnFe-TOS compared to the MnFe-TiO₂ catalyst. Combining with the Ti2p

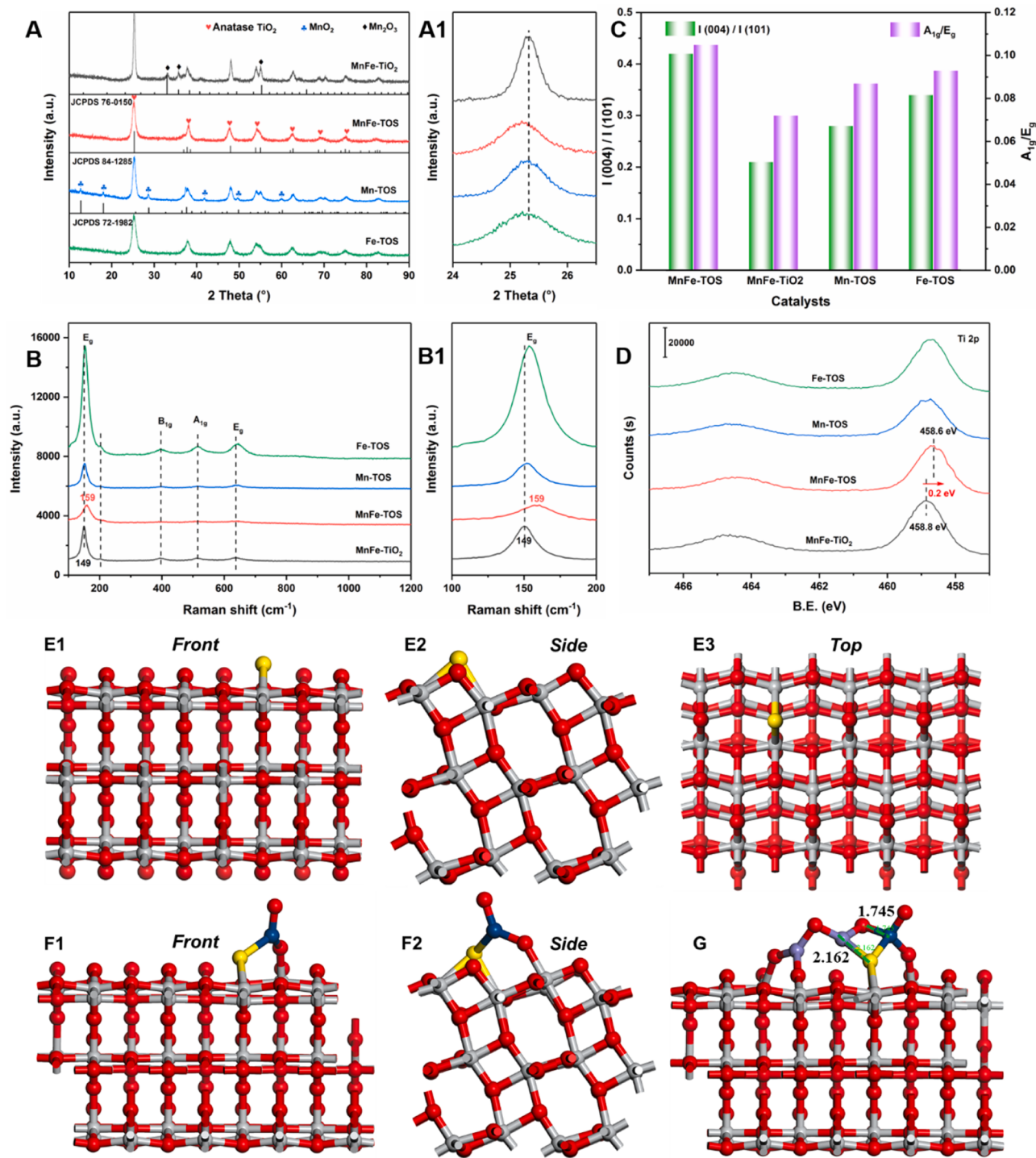


Fig. 3. XRD patterns (A, A1), Raman spectra (B, B1), histogram of peaks intensity ratio from XRD and Raman (C), Ti2p fine spectra (D), DFT computational optimized structure of S-TiO₂(101) (E1–3), MnO₂/S-TiO₂(101) (F1, 2), and Fe₂O₃-MnO₂/S-TiO₂(101) (G), red ball: O, gray ball: Ti, yellow ball: S, cyan ball: Mn, and purple ball: Fe.

spectrum of pure TiOSO₄ in Fig. S2A, it could be confirmed that the introduction of SO₄²⁻ with stronger electronegativity into the TiO₂ lattice changed the surrounding electronic environment. Furthermore, spent catalysts after NH₃-SCR reaction were also analyzed and corresponding results were depicted in Fig. S2C and Figs. S3–4, the pre-sulfurized TiO₂ structure remain stable after the NH₃-SCR reaction.

The TEM and HRTEM images of MnFe-TOS and MnFe-TiO₂ were presented in Fig. S5. As for the MnFe-TOS, the inset in Fig. S5A showed clear diffraction rings, and only lattice stripes with $d_{(101)}$

= 0.35–0.36 nm of anatase TiO₂ were observed in Fig. S5B, the large lattice spacing further confirmed the lattice expansion of TiO₂ due to the insertion of SO₄²⁻. In contrast, as shown in the inset in Fig. S5C, diffraction rings and diffraction spots coexisted on the MnFe-TiO₂ catalyst, verifying the coexistence of polycrystalline large particles of TiO₂ and Mn₂O₃, which was in high agreement with the XRD results. It should be noted that in addition to the lattice stripes of the TiO₂ (101) crystal plane ($d=0.35$ nm), lattice stripes of the TiO₂ (004) crystal plane ($d=0.24$ nm) as well as the Mn₂O₃ (110) crystal plane ($d=0.66$ nm) could also be

Table 2

Crystal size and specific peaks intensity ratio from XRD and Raman.

Samples	Crystal size (nm) ^a	$I_{(004)} / I_{(101)}$ ^b	A_{1g} / E_g ^c
MnFe-TOS	9.0	0.42	0.105
MnFe-TiO ₂	19.0	0.21	0.072
Mn-TOS	10.5	0.28	0.087
Fe-TOS	6.9	0.34	0.093

^a calculated by FWHM from XRD.^b calculated by peak intensity from XRD.^c calculated by peak intensity from Raman.

observed in Fig. S5D, implying that the crystal structure of MnFe-TiO₂ and MnFe-TOS may be different. For this reason, necessary calculations about the intensity ratio of A_{1g}/E_g in the Raman spectrum and $I_{(004)}/I_{(101)}$ in the XRD patterns have been done, and the results were shown in Table 2 and Fig. 3C. It could be easily found that both the ratio value of $I_{(004)}/I_{(101)}$ and A_{1g}/E_g followed the sequence: MnFe-TOS > Fe-TOS > Mn-TOS > MnFe-TiO₂, indicating that the MnFe-TOS exposed more lattice defects because of the lattice distortion induced by the insertion of SO₄²⁻ into TiO₂.

Pore structure was analyzed by N₂ ad-desorption experiments. As illustrated in Fig. S6A, both of MnFe-TOS and MnFe-TiO₂ showed IV adsorption isotherm (IUPAC), but the desorption hysteresis loops were different from each other. Typically, the MnFe-TOS owned H2 hysteresis loop, while the MnFe-TiO₂ possessed H3 hysteresis loop. In terms of the pore size distribution in Fig. S6B, two different pore diameters of 7.3 nm and 10.0 nm were mainly present on the MnFe-TOS, while pore diameter of 9.0 nm was mainly present on MnFe-TiO₂. The specific surface area (S_{BET}) was listed in Table 3, it could be found that the S_{BET} of MnFe-TOS (100.8 m²/g) was slightly higher than that of MnFe-TiO₂ (92.1 m²/g). Since the larger specific surface area facilitates the high dispersion of Fe/Mn species, the MnFe-TOS catalyst would provide more reactive sites. Comparing the changes of catalyst specific surface area and pore structure before and after the SO₂-resistance test, it was easy to find that the specific surface area of both MnFe-TOS and MnFe-TiO₂ catalysts decreased, but the decrement of MnFe-TiO₂ catalyst ($\Delta S_{BET}=38.4$) was more serious than that of the MnFe-TOS ($\Delta S_{BET}=16.8$) shown in Fig. S6C. Similar trends were also observed on pore volume (ΔV) and average pore diameter (ΔD). These changes might be closely related to the deposition of different amounts of sulfates on the catalyst surface, which would be discussed further later.

3.4. Exploration of the sulfur species

The hydrolysis of TiOSO₄ and the addition of MnSO₄ during the catalyst synthesis process could directly introduce sulfur into the fresh MnFe-TOS catalyst system, and new sulfur species would be deposited on the spent catalyst surface after the SO₂-resistance test, so it is necessary to explore sulfur species in the fresh and spent catalysts. Firstly, the total S content was quantified by ICP-OES and the results were listed in Table S1. It could be found that the fresh MnFe-TOS

contained a certain amount S (0.9%), and that of the MnFe-TiO₂ was almost negligible (0.2%). Combining with the S2p spectrum of TiOSO₄ in Fig. S2B, it suggested that TiOSO₄ hydrolysis was more likely to introduce S into fresh catalyst than direct addition of MnSO₄. After SO₂-resistance test, both of the spent catalysts MnFe-TOS-S and MnFe-TiO₂-S possessed same S content (1.8%). As compared in Fig. 4A, it could be easily calculated that the deposition of sulfur species after SO₂-resistant test on MnFe-TOS-S (0.9%) was significantly lower than that on MnFe-TiO₂-S (1.6%). Subsequently, surface atomic concentrations of S on fresh and spent catalysts were also characterized by XPS. As listed in Table 4, fresh catalysts obtained from TiOSO₄ hydrolysis, such as MnFe-TOS, Mn-TOS, and Fe-TOS, showed higher surface S content than the MnFe-TiO₂. Comparing to the sulfur content on spent catalysts surface after the SO₂-resistance test, as depicted in Fig. 4B, the deposition of sulfur species after SO₂-resistant test on the surface of MnFe-TiO₂-S was significantly higher than that of MnFe-TOS-S, which was consistent well with the ICP results.

The valence state of sulfur species can be confirmed through the S 2p fine spectrum. As shown in Fig. 4C, except for the MnFe-TiO₂, all of the MnFe-TOS, Fe-TOS and Mn-TOS detected significant S 2p signal peaks. Typically, the S 2p fine spectrum could be deconvoluted into S 2p_{3/2} and 2p_{1/2} of sulfate [13,21]. It could be found that the Fe-TOS showed the strongest S 2p signal, followed by MnFe-TOS and Mn-TOS, this indicated that Fe has a larger capacity for S than Mn, which should be the main reason why Fe-TOS has better SO₂ resistance than Mn-TOS. After SO₂-resistance test, the S 2p fine spectra of spent catalysts MnFe-TOS-S and MnFe-TiO₂-S were also collected in Fig. 4D. Since almost no signal of S 2p was detected on fresh MnFe-TiO₂ catalyst, large amounts of sulfates were detected on the spent MnFe-TiO₂-S surface. Compared with fresh catalyst, the deposition of sulfate after SO₂-resistant test on the surface of MnFe-TiO₂-S was significantly greater than that of MnFe-TOS-S. Based on the changes in specific surface area in Table 3, it could be seen that a large amount of sulfate deposition blocked some of the MnFe-TiO₂-S pores, resulting in a decrease in its specific surface area.

Sulfur species on spent catalysts MnFe-TOS-S and MnFe-TiO₂-S were further characterized by TG-DSC and the result was shown in Fig. S7. The weight loss process of spent catalysts (MnFe-TiO₂-S and MnFe-TOS-S) could be divided into three steps. Step I (<240 °C) was attributed to the desorption of absorbed water and other impurities. Step II (240–670 °C) could be taken as the decomposition of (NH₄)₂SO₄ and NH₄HSO₄. It should be pointed out that ammonium sulfate salt deposited on both of MnFe-TiO₂-S and MnFe-TOS-S were relatively weak, which should be related to the coexistence of Mn-Fe dual active sites. The step III (670–800 °C) showed a sharp weight loss with a distinct endothermic peak was assigned to the decomposition of metal sulfates [27], it could be found that the weight loss of MnFe-TiO₂-S (4.3%) above 670 °C was higher than MnFe-TOS-S (3.0%). This phenomenon indicated that the metal sites on the MnFe-TiO₂ catalyst surface were more susceptible to SO₂ attack, which would have a negative impact on its NH₃-SCR activity.

Based on above analysis results of ICP, XPS, and TG-DSC, we concluded that a certain amount of SO₄²⁻ has been pre-implanted in the fresh MnFe-TOS catalyst, which could inhibit the deposition of surface sulfate during the SCR reaction to some extent, thus exhibiting better SO₂-resistance than MnFe-TiO₂ catalyst. However, which active sites on MnFe-TOS and MnFe-TiO₂ were attacked by the sulfur species after the reaction were still not clear. Taking this point into consideration, it is necessary to investigate the valence states of different metal oxides as well as catalysts surface chemical environment.

3.5. Surface chemical environment analysis

The exploration for surface electronic states of fresh and spent catalysts was conducted by XPS, corresponding fine spectra of O 1 s, Fe 2p, Mn 2p were collected in Fig. 5, and surface composition proportions

Table 3

BET surface area and pore structure properties.

Samples	BET Surface Area (m ² /g)	ΔS_{BET}	Pore Volume (cm ³ /g)	ΔV	Pore Diameter (nm)	ΔD
MnFe-TOS	100.8	16.8	0.31	0.03	9.51	-1.04
MnFe-TOS-S	84.0		0.28		10.55	
MnFe-TiO ₂	92.1	38.4	0.38	0.12	12.81	-2.80
MnFe-TiO ₂ -S	53.7		0.26		15.61	

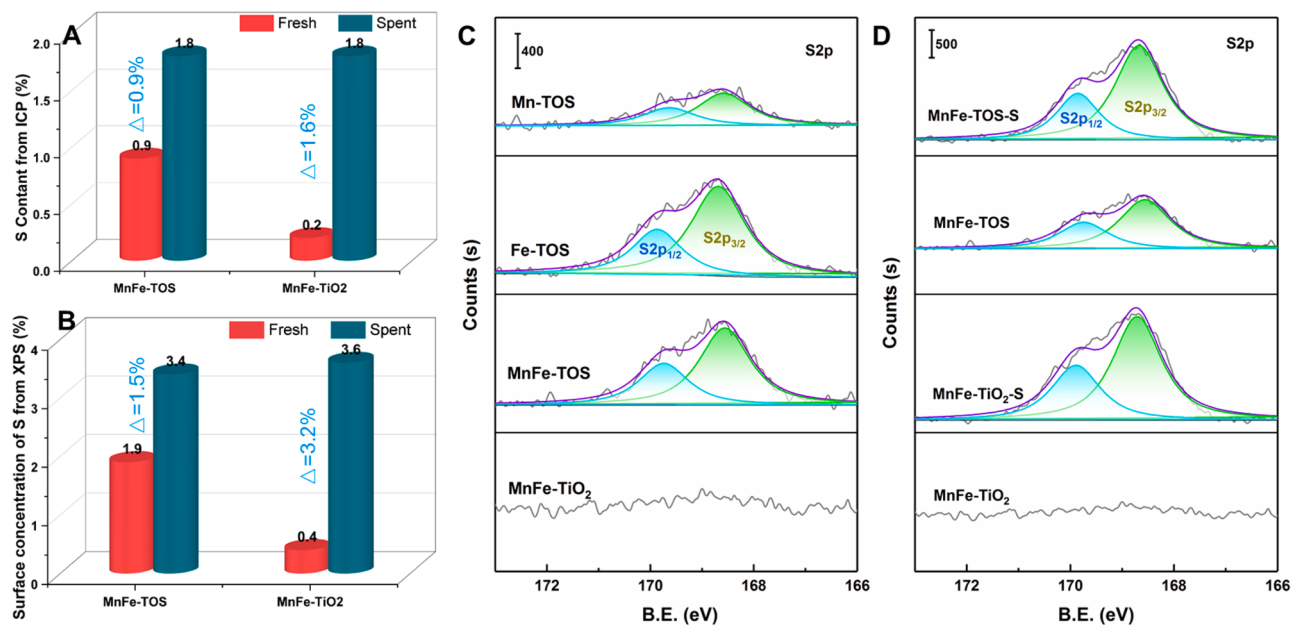


Fig. 4. Histogram of S contents form ICP (A) and XPS (B), S2p fine spectra of fresh and spent catalysts (C, D).

Table 4
Catalysts surface composition proportion from XPS results (%).

Samples	Surface atomic concentrations (%)					Relative concentration ratios (%)				
	Fe	Mn	O	Ti	S	Fe ³⁺	Mn ⁴⁺	Mn ³⁺	Mn ²⁺	O _a
MnFe-TOS	6.1	6.8	65.4	19.8	1.9	43.9	23.2	34.7	42.1	22.6
MnFe-TiO ₂	6.7	8.0	63.7	21.2	0.4	45.1	31.5	34.3	34.2	8.5
Mn-TOS	-	7.9	65.6	25.3	1.2	-	26.3	35.2	38.5	13.1
Fe-TOS	4.3	-	67.3	25.8	2.6	45.0	-	-	-	21.2
MnFe-TOS-S	5.0	6.0	67.2	18.4	3.4	46.4	23.4	33.3	43.3	36.0
MnFe-TiO ₂ -S	5.8	6.1	65.9	18.6	3.6	49.1	24.8	39.1	36.0	32.3

were listed in Table 4. As shown in Fig. 5A, Fe 2p peaks were obviously detected on the Fe-TOS, MnFe-TOS and MnFe-TiO₂, where Fe³⁺ coexisted with Fe²⁺ [28]. Despite the identical valence distribution of Fe (Table 4), the peaks position of the Fe-TOS and MnFe-TOS shifted toward higher binding energy compared to that of the MnFe-TiO₂, indicating that a strong metal-support interaction between Fe and TOS have occurred on the Fe-TOS and MnFe-TOS. The Mn 2p_{3/2} peak in Fig. 5B could be deconvoluted into Mn⁴⁺ (643.9 eV), Mn³⁺ (642.6 eV), and Mn²⁺ (641.5 eV) [14]. It could be easily found that the proportions of Mn⁴⁺ in MnFe-TOS (23.2%) and Mn-TOS (26.3%) were much lower than that of the MnFe-TiO₂ (31.5%), indicating that large amount of SO₄²⁻ doping disturbed the local electronic environment lowering the oxidation state of Mn, which would further affect the redox capacity of the catalyst. Comparing with Mn-TOS, the addition of Fe further accelerated the reduction of Mn⁴⁺ → Mn³⁺ → Mn²⁺ in MnFe-TOS. The reduced oxidation state of Mn on MnFe-TOS allowed the inhibition of SO₂ oxidation and NH₃ peroxidation, which was well consistent with its strong tolerance to SO₂ and high N₂ selectivity. Above analysis confirmed that strong interaction occurred on the MnFe-TOS where Mn-Fe species highly dispersed in amorphous phase. In contrast, the electron transfer between isolated Mn₂O₃ and Fe sites on MnFe-TiO₂ was relatively difficult.

O 1 s spectra in Fig. 5C could be divided into lattice oxygen (O_β: 530.1 eV) and chemisorbed oxygen from oxide defects or hydroxyl-like groups (O_a: 531.4–531.7 eV) [23]. As described in Fig. 5D, it could be found that the O_a ratio of MnFe-TOS (22.6%) was much higher than the MnFe-TiO₂ (8.5%). Generally speaking, the chemisorbed oxygen is closely related to catalyst redox property and is beneficial for SCR

reactions [29]. However, this may not be true for pre-sulfated catalysts in this work because some contribution of O_a should come from the oxygen in S=O and S-OH, similar phenomenon has also been reported by other reports [7,30]. That is to say, the introduction of S atoms via pre-sulfurization leads to lattice distortion of TiO₂ and some of oxygen vacancies have been occupied by SO₄²⁻ in MnFe-TOS, which resulted in a decrease in active oxygen and loss of low-temperature catalytic activity compared with the MnFe-TiO₂. Besides, the O 1 s signal counts of MnFe-TOS were higher than both of Mn-TOS and Fe-TOS, which indicated that the co-existence of Mn and Fe could generate more surface absorbed oxygen.

After SO₂-resistance test, the variations on the surface chemical environment of spent catalysts MnFe-TOS-S and MnFe-TiO₂-S were also detected. As illustrated in Fig. 6A-A1, a significant increase in the O_a proportion was observed on the MnFe-TiO₂-S, which was mainly from the deposited surface sulfate species, such as the oxygen in S=O and S-OH [30]. In contrast, the incremental percentage of O_a on MnFe-TOS-S was relatively less, indicating that oxygen species on MnFe-TOS maintained dynamic equilibrium during the reaction process. Importantly, the variation of Mn and Fe valence states on fresh and spent catalysts were compared and discussed. As shown in Fig. 6B-B1, the proportion of Fe³⁺ on MnFe-TOS-S and MnFe-TiO₂-S had slightly increased, indicating that there should be the formation of Fe₂(SO₄)₃. Interestingly, the valence state changes of Mn on MnFe-TOS-S and MnFe-TiO₂-S were not entirely the same in Fig. 6C-C1. Typically, the proportion of Mn⁴⁺, Mn³⁺, and Mn²⁺ on MnFe-TOS-S almost unchanged compared to fresh MnFe-TOS. However, an obvious decline of Mn⁴⁺ ratio (from 31.5% to 24.8%) was observed on MnFe-TiO₂-S compared to

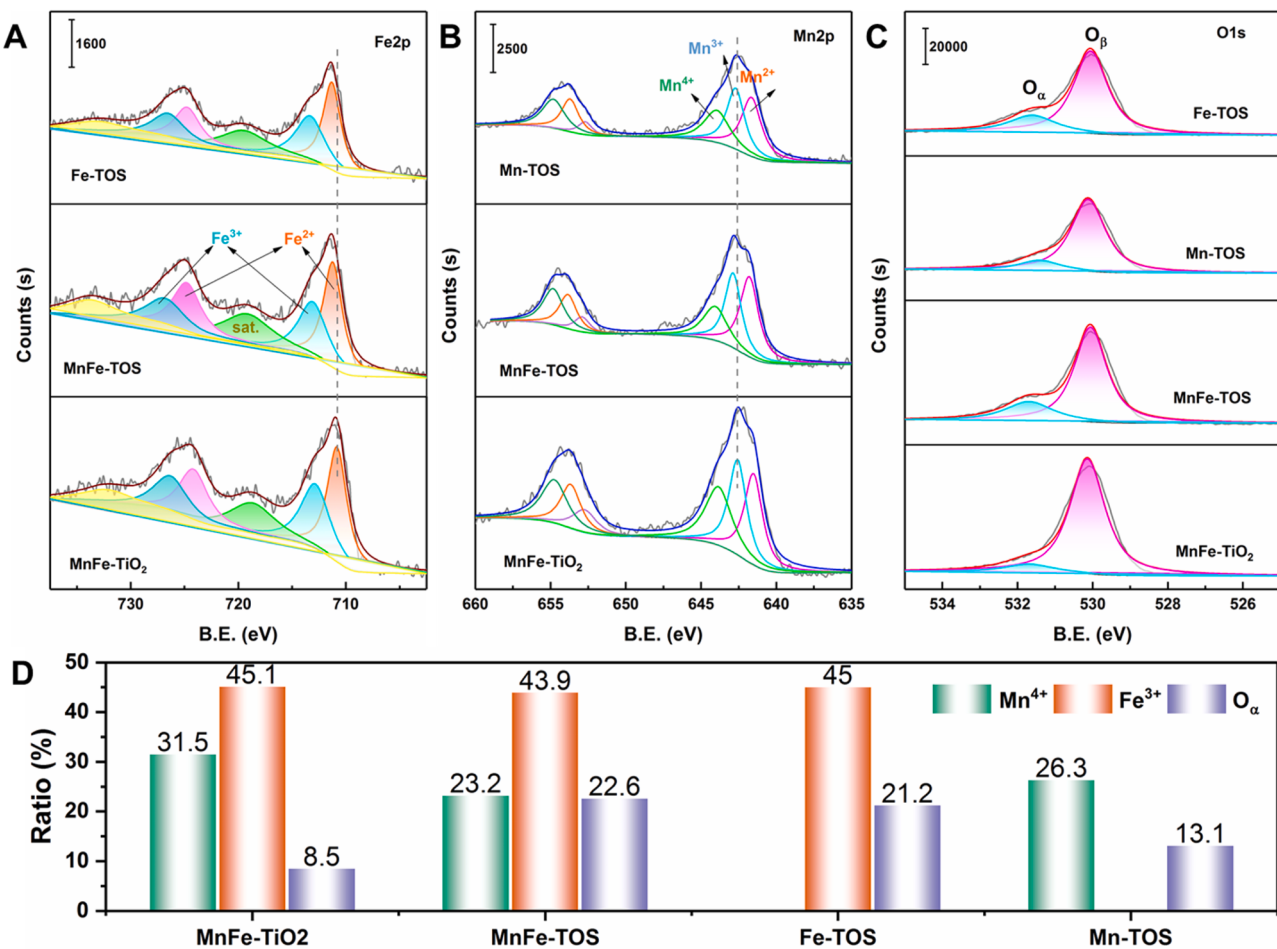


Fig. 5. XPS spectra of Fe2p (A), Mn2p (B), O1s (C), and histogram of valence states ratio for different elements (D).

fresh MnFe-TiO₂ accompanied with increasement of Mn³⁺ (from 34.3% to 39.1%) and Mn²⁺ ratio (from 34.2% to 36.0%), implying the formation of Mn₂(SO₄)₃ and MnSO₄ on MnFe-TiO₂-S. Above phenomenon revealed that the isolated Mn sites on MnFe-TiO₂ could be easily attacked by electron-rich SO₂ to form manganese sulfates, which blocked the charge transfer between active sites during the NH₃-SCR process and led to MnFe-TiO₂ catalyst poisoning and deactivation. Comfortingly, benefitting from the pre-sulfurization as well as strong interaction between Mn and Fe on the MnFe-TOS, SO₂ adsorption behavior was inhibited, thus protecting the Mn site from being affected and ensuring electronic cycling during the NH₃-SCR process, thus exhibiting good SO₂ resistance.

3.6. Redox ability

H₂-TPR profiles were generally used for determining the reducibility of catalysts. As illustrated in Fig. 7A, a strong peak at 465 °C accompanied with a weak peak at 533 °C appeared on the Fe-TOS, which were contributed to the reduction of Fe₂O₃ → Fe₃O₄ → FeO [31,32]. For the Mn-TOS, the overlapped reduction peaks at 300–500 °C and the symmetrical peak appeared at 573 °C were attributed to the sequential reduction of Mn⁴⁺ → Mn³⁺ → Mn²⁺ [33,34]. In terms of the MnFe-TOS, a broad peak before 400 °C was the reduction of amorphous MnO_x, which was easier reduced than crystal MnO₂. Besides, the sharp peak at 476 °C should be contributed to the reduction of Fe–O–Mn since strong interaction existed between highly dispersed Mn/Fe species [23]. However, the H₂-TPR profile of MnFe-TiO₂ was greatly different from that of MnFe-TOS, where the overlapped reduction peaks were observed at 200–700 °C. In detail, a small peak at 385 °C with a shoulder peak

around 430 °C were corresponding to the reduction of Fe³⁺ → Fe²⁺, while other H₂ consumption peaks below 350 °C and above 500 °C were assigned to the reduction of isolated crystalline Mn₂O₃ and other manganese oxide species. That is, the Mn/Fe species on the MnFe-TiO₂ catalyst existed separately and interaction effect were weak.

Besides, the light-off temperature on H₂-TPR curves is another important indicator reflecting the catalytic activity. As marked in Fig. 7A, the light-off temperatures of Fe-TOS, Mn-TOS, MnFe-TOS and MnFe-TiO₂ were 340 °C, 260 °C, 210 °C and 150 °C, respectively. Generally speaking, lower light-off temperature implied easier reduced and the greater redox ability, which were consistent well with the low-temperature catalytic activities followed the sequences: Fe-TOS < Mn-TOS < MnFe-TOS < MnFe-TiO₂. Besides, the H₂-TPR curves were calibrated by the reduction of pure CuO, corresponding results were collected in Table S2, the H₂ consumption of each catalyst also followed the above ranking results. To sum up, the intercalation of SO₄²⁻ into MnFe-TOS could inhibit the reducibility compared to MnFe-TiO₂, but the strong interaction between Mn–O–Fe induced by interfacial confinement effect was supposed to be conducive to its catalytic activity and stability.

3.7. Adsorption properties

Catalysts surface acid properties were investigated via NH₃-TPD in Fig. 7B. All desorption curves could be divided into three regions according to temperature. Typically, the region I below 200 °C was assigned to the weakly adsorbed NH₃ on weak acid sites, region II among 200–325 °C was ascribed to medium acid sites, and the region III above 325 °C corresponded the strong acid sites [35]. By integrating the area

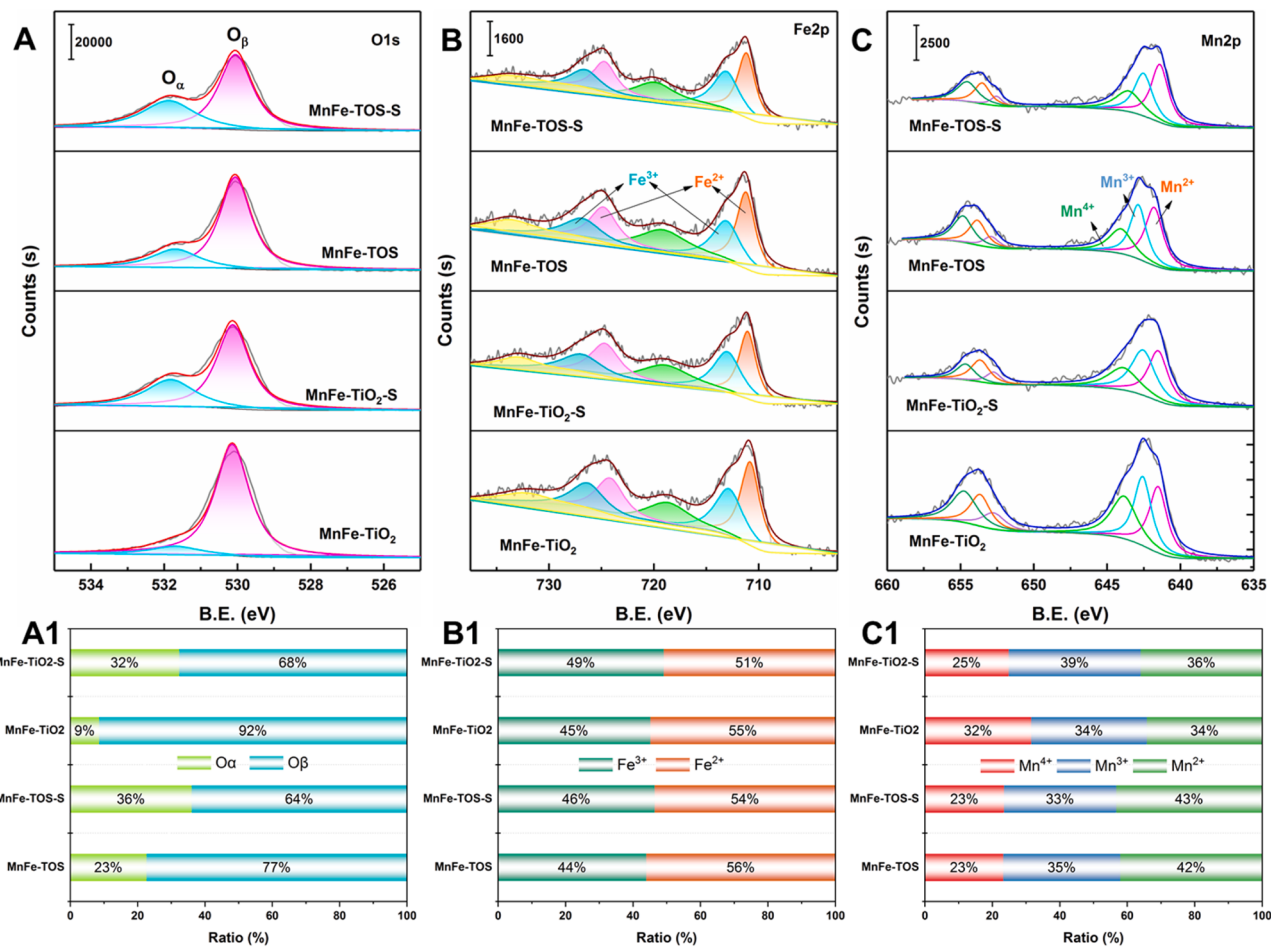


Fig. 6. XPS curves and valence changes of spent catalysts MnFe-TOS-S and MnFe-TiO₂-S.

of desorption curves, the statistics were shown in Fig. S8, the more NH₃ desorbed over the catalyst, the more acid sites it owned on the surface. It could be found that Fe-TOS possessed the largest amount of acid sites, in the following order of MnFe-TOS, MnFe-TiO₂, and Mn-TOS. Compared to MnFe-TiO₂, the abundance of surface acid sites on MnFe-TOS should be related to the existence of SO₄²⁻ since literatures have reported that sulfate would create additional more acidic sites [13,36]. It could be easily found that the most significant difference between the MnFe-TOS and MnFe-TiO₂ was that MnFe-TOS possessed a large number of strong acid sites. Combined with the results of XPS analysis, it could be seen that the SO₄²⁻ originated from TiOSO₄ hydrolysis during the synthesis of MnFe-TOS disturbed the local electronic environment and generated more surface acid sites. Herein, we could conclude that strong surface acidity broadened MnFe-TOS operating temperature window in NH₃-SCR.

Additionally, SO₂ adsorption capacity of catalysts were evaluated via SO₂-TPD. As depicted in Fig. 7C, the desorption curves could be divided into three stages, corresponding to physical adsorbed SO₂ (<150 °C), chemisorbed SO₂ (150–350 °C), and sulfates decomposition (>450 °C) [27,37]. By counting the integrated area of the desorption curves in Fig. 7D, it was easy to find that the SO₂ adsorption capacities of Fe-TOS and Mn-TOS were much higher than that of MnFe-TOS and MnFe-TiO₂, which indicated that the efficient charge transfers between Mn and Fe significantly inhibited SO₂ oxidation and sulfates generation, and weakened the SO₂ poisoning effect. However, compared to Mn-TOS, the bonding strength of chemisorbed SO₂ on Fe-TOS was weaker and complete desorption could be achieved at relatively lower temperatures. This could well explain why Fe-TOS showed better SO₂-resistance than Mn-TOS (Fig. 1E). Except for a slight increase in weakly physiosorbed

SO₂ (which was mainly related to the large specific surface area), the strong chemisorbed SO₂ as well as sulfates on the MnFe-TOS were significantly less than that of MnFe-TiO₂. Thus, it could be concluded that pre-sulfurization during synthesis process for the MnFe-TOS could effectively inhibit the strong chemisorption of SO₂ and the generation of sulfates during the catalytic reaction, thus weakening the SO₂ poisoning effect and exhibiting better SO₂ resistance than conventional MnFe-TiO₂ catalyst.

O₂-TPD is the most effective way to evaluate the adsorption and activation ability of oxygen species of the catalysts. As shown in Fig. 7E, an O₂ desorption peak appeared below 300 °C was attributed to surface adsorbed oxygen (α) on oxygen-vacancy, and successive desorption peaks in the range of 300–650 °C were belong to O²⁻ stripped from lattice oxygen sites (β) [13,38]. As mentioned earlier in XPS O1s spectra, as well as the XRD and Raman results, the MnFe-TOS should have more oxygen vacancies due to lattice distortion. However, here O₂-TPD results showed that the adsorbed oxygen species on MnFe-TOS were not significantly increased compared to that of MnFe-TiO₂. This further supported the speculation that some of the oxygen vacancies were occupied by SO₄²⁻, which also explained the fact that the low-temperature activity of MnFe-TOS was not as good as that of MnFe-TiO₂ below 200 °C. Finally, a distinct desorption peak observed among 650–800 °C should be related with the desorption SO₂ (γ) from sulfate decomposition [13]. To confirm this hypothesis, He-TPD was also performed on all fresh catalysts. As shown in Fig. S9, similar desorption peaks appeared above 650 °C. It could be found that sulfate decomposition peaks intensity of MnFe-TOS, Mn-TOS, and Fe-TOS was much higher than that of MnFe-TiO₂, which confirmed that hydrolysis of TiOSO₄ during catalyst synthesis provided a large amount of SO₄²⁻ and

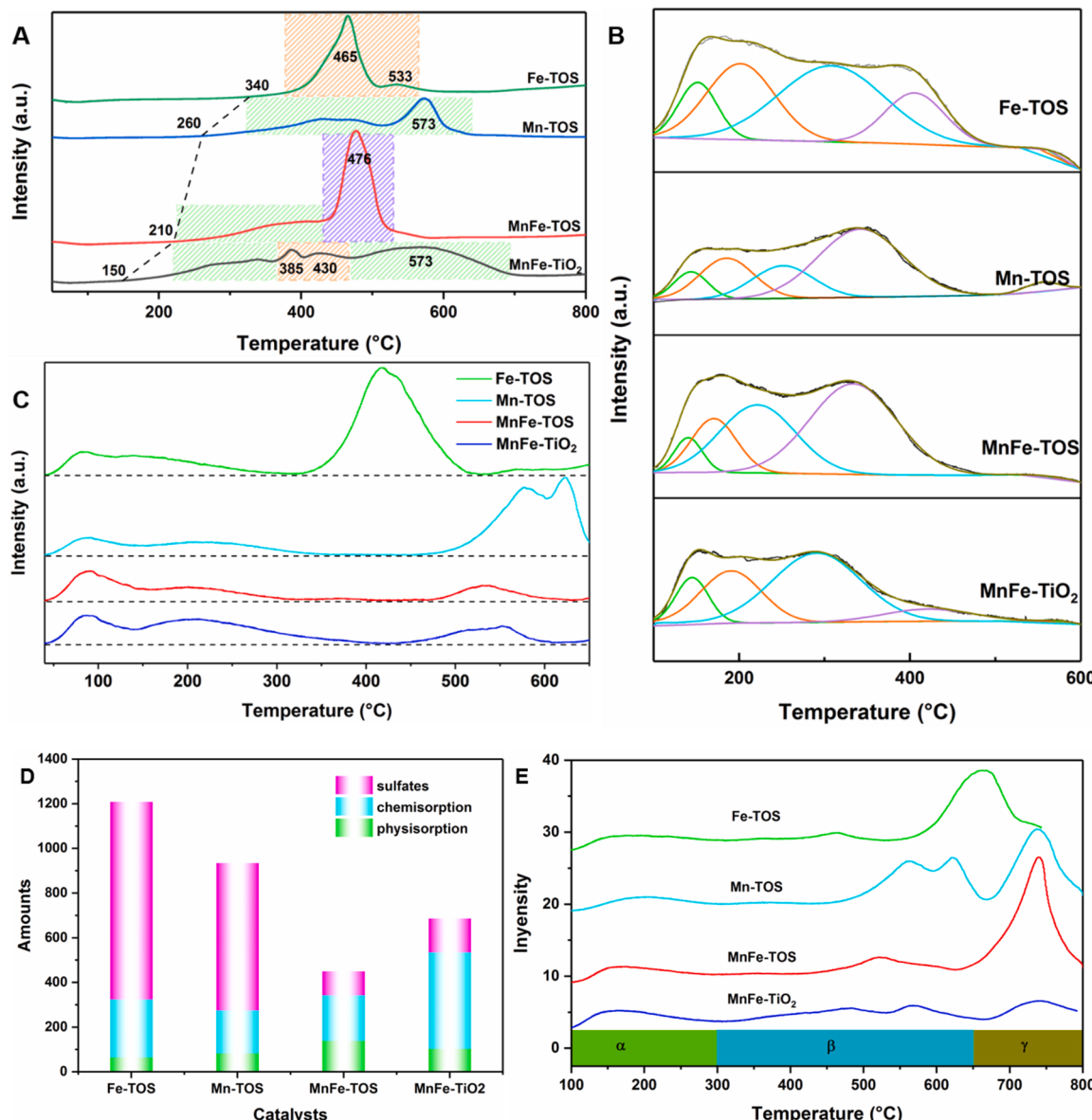


Fig. 7. H₂-TPR profiles (A), NH₃-TPD (B), SO₂-TPD (C), histogram of different sulfur species (D), and O₂-TPD (E).

interposed into TOS support. Besides, a clear desorption peak was observed on MnFe-TOS near 200 °C, it confirmed that SO₄²⁻ occupied some of the oxygen vacancies in the MnFe-TOS, resulting in a decrease in the amount of active oxygen on the surface, which well explained the fact that the low-temperature activity of MnFe-TOS was not as good as that of MnFe-TiO₂ below 200 °C. In summary, occupation of some oxygen vacancies by SO₄²⁻, although inhibiting the redox capacity of the MnFe-TOS, significantly inhibited the adsorptive oxidation of SO₂ and improved the N₂ selectivity, thus the overall beneficial effect on the MnFe-TOS catalytic performance outweighed the detrimental effect.

4. Reaction mechanism study

To investigate the reaction mechanism of NH₃-SCR, the adsorption behavior of the reactants on the catalyst surface and the reaction process were studied using *in situ* DRIFTS. Competitive adsorption experiments for NH₃ and NO + SO₂ + O₂ on MnFe-TOS and MnFe-TiO₂, and transient reaction experiments including NO + SO₂ + O₂ react with pre-adsorbed NH₃, as well as NH₃ reacts with pre-adsorbed NO + SO₂ + O₂ were all carried out on MnFe-TOS and MnFe-TiO₂.

4.1. Reactant adsorption behaviors

In-situ DRIFTS spectra for NH₃ adsorption at 50 °C on MnFe-TOS and MnFe-TiO₂ were collected in Fig. 8A and B, respectively. With the progression of adsorption time, the bands at 1475 cm⁻¹, 1406 cm⁻¹ as well as 1690–1940 cm⁻¹ were assigned to the bending vibration of NH₄⁺ species on Brønsted acid sites [39]. Bands at 1597 and 1265 cm⁻¹ were corresponded to the bending vibration of the N-H bonds in NH₃ linked to Lewis acid sites [40], and the band at 1170 cm⁻¹ also was ascribed to NH₃ coordinately linked to Lewis acid sites [41]. It was easily found that ammonia species were more likely adsorbed on the Brønsted acid site of MnFe-TOS at 50 °C to form a large amount of NH₄⁺, while NH₃ tended to be adsorbed on the Lewis acid site on MnFe-TiO₂ in addition to a large amount of NH₄⁺ bonded on the Brønsted acid site.

Comparably, NH₃ adsorption on MnFe-TOS and MnFe-TiO₂ at 200 °C were also conducted and corresponding *in-situ* DRIFTS spectra were collected in Fig. 8C and D, respectively. Taking MnFe-TOS as an example, NH₄⁺ species on Brønsted acid sites bending vibration bands were detected at 1469 cm⁻¹, 1406 cm⁻¹ and 1693 cm⁻¹, while strong bands appeared at 1597 cm⁻¹ and 1251 cm⁻¹ corresponding to

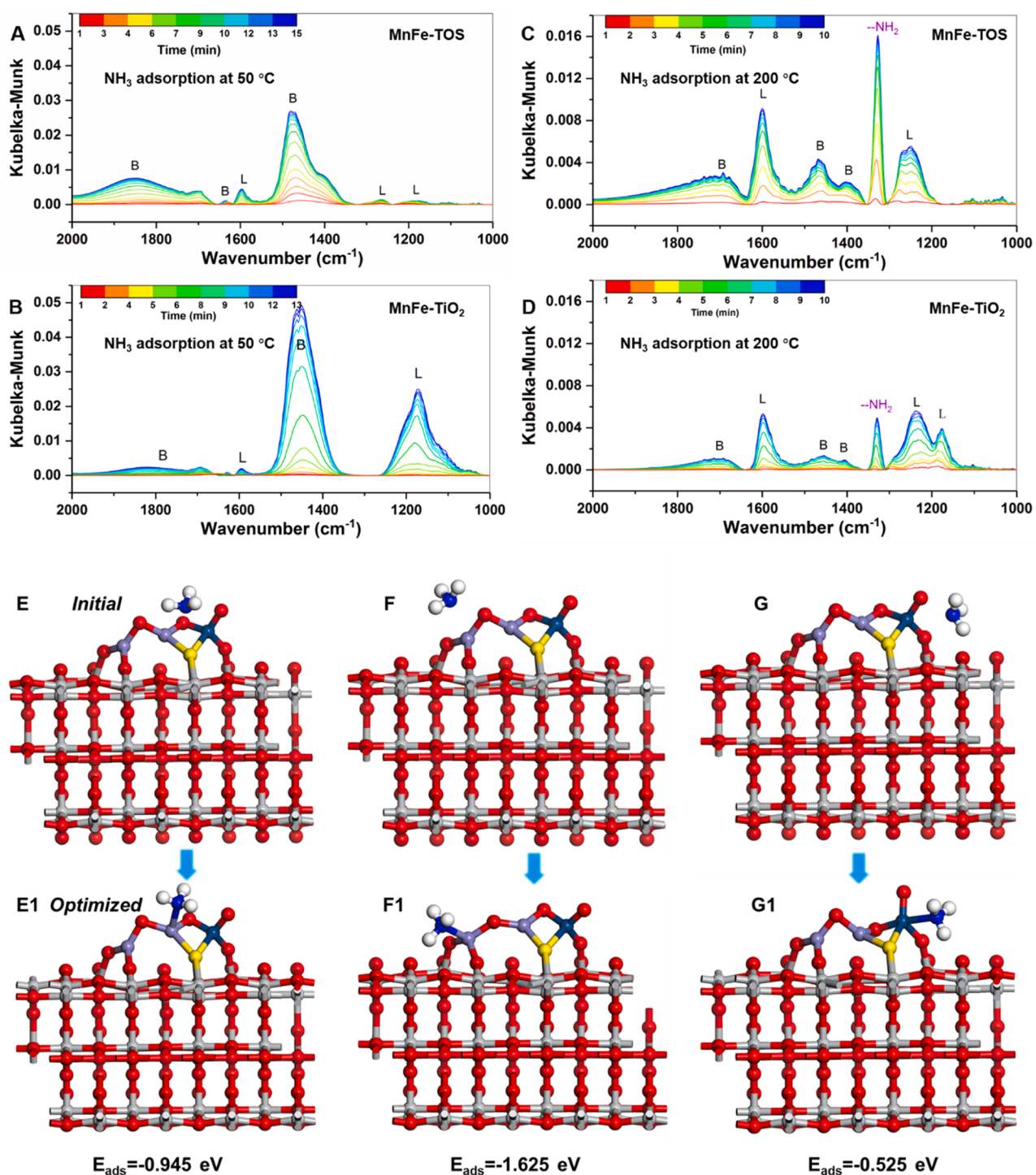


Fig. 8. In-situ DRIFTS of NH₃ adsorption on MnFe-TOS and MnFe-TiO₂ at 50 °C (A, B), and 200 °C (C, D). The different NH₃ adsorption model and adsorption energy on MnFe-TOS (E-G), red ball: O, gray ball: Ti, yellow ball: S, cyan ball: Mn, purple ball: Fe, white ball: H, and blue ball: N.

coordinately adsorbed to Lewis acid sites. Notably, a new band appeared at 1326 cm⁻¹ should be affiliated to the scissoring vibration -NH₂ species, which suggested that NH₃ coordinately linked to Lewis acid sites were readily activated at 200 °C [42,43]. Similar phenomenon could also be found on the MnFe-TiO₂ (Fig. 8D), but the bands intensity of -NH₂ species at 1326 cm⁻¹ was distinctly weaker than that of the MnFe-TOS, implying that MnFe-TOS has a much stronger activation capacity for NH₃ than MnFe-TiO₂. In addition, an interesting phenomenon on MnFe-TOS worth mentioning is that the adsorption capacity of ammonia on Lewis acid sites was significantly enhanced while that on

Brønsted acid sites dramatically weakened. However, a serious decrease in the adsorption capacity of both Brønsted acid sites and Lewis acid sites for ammonia species was observed on the MnFe-TiO₂. That is, there is a huge difference in the variation of ammonia adsorption capacity on different types of acid sites on the MnFe-TOS and MnFe-TiO₂ under high and low temperature conditions. The strong adsorption and activation ability of ammonia is an important guarantee condition for the excellent catalytic activity of the MnFe-TOS at 200 °C.

Competitive adsorption of SO₂ and NO+O₂ experiments were also carried out on MnFe-TOS and MnFe-TiO₂ at 50 °C. As for the MnFe-TOS

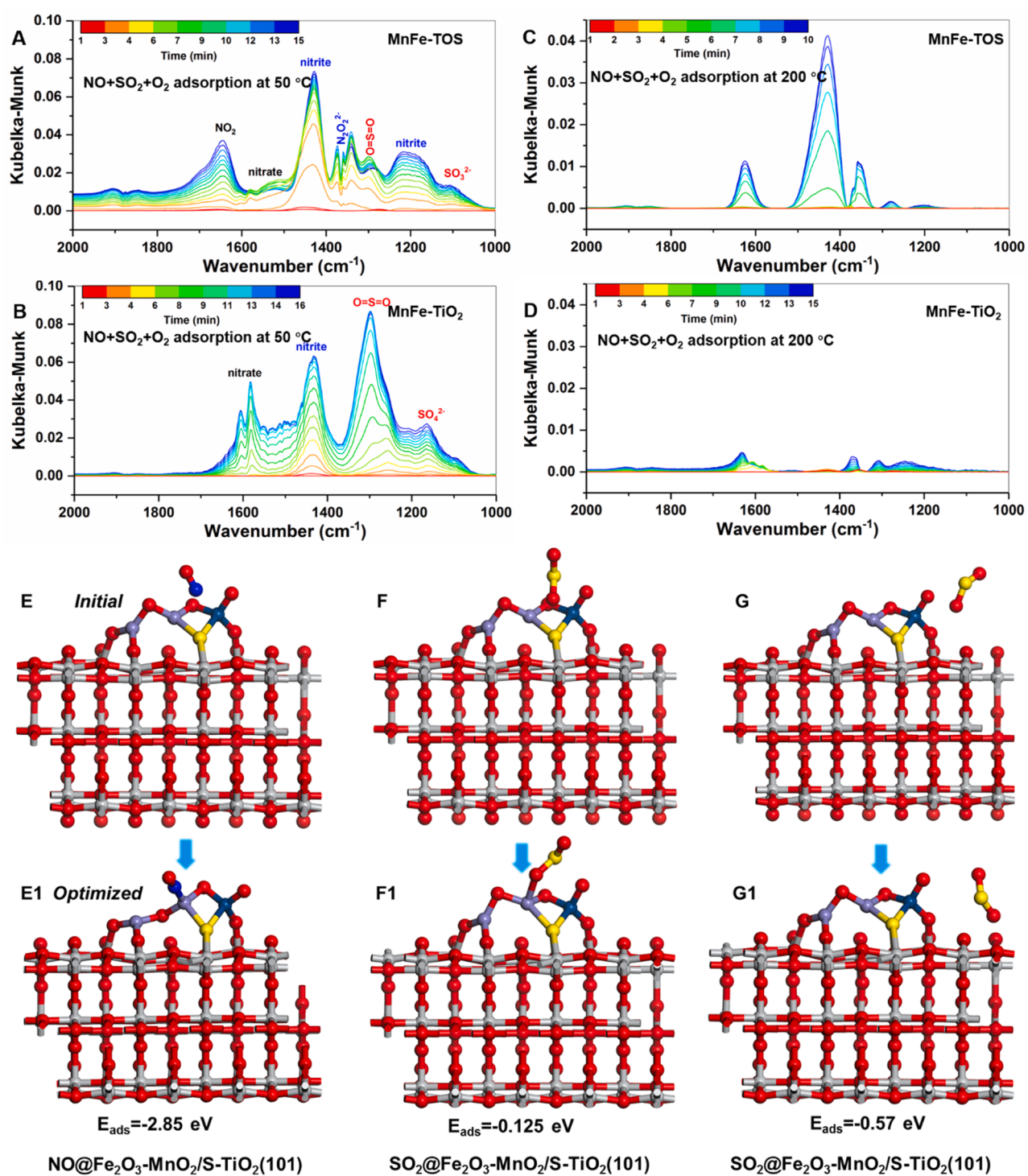


Fig. 9. In-situ DRIFTS of NO+SO₂+O₂ adsorption on MnFe-TOS and MnFe-TiO₂ at 50 °C (A, B), and 200 °C (C, D). The adsorption model and adsorption energy on MnFe-TOS of NO (E1, 2), and SO₂ (F-G), red ball: O, gray ball: Ti, yellow ball: S, cyan ball: Mn, purple ball: Fe, and blue ball: N.

(Fig. 9A), the band at 1645 cm⁻¹ was ascribed to the adsorbed NO₂ [8], and the bands at 1580 and 1517 cm⁻¹ were assigned to bidentate nitrates [44]. The strong band at 1429 cm⁻¹ related to nitrite species, and several small bands at 1373, 1340, and 1360 cm⁻¹ corresponded to chelating nitrite and N₂O₂²⁻ [7]. The broad band at 1200 cm⁻¹ was due to bridging nitrite [31]. Besides, the bands at 1298 cm⁻¹ can be ascribed to surface SO₂ (O=S=O), and the bands at 1098 cm⁻¹ belonged to sulfites [45]. Compared with the MnFe-TiO₂ in Fig. 9B, the adsorbed NO₂, N₂O₂²⁻, and chelating nitrite were not detected. Instead, more

monodentate nitrite (1606 cm⁻¹) and bidentate nitrate (1580 cm⁻¹) were appearing [7]. It should be pointed out that the band at 1298 cm⁻¹ due to O=S=O and 1164 cm⁻¹ of SO₄²⁻ appeared on MnFe-TiO₂ and became stronger with the increasing exposure time [8]. Above phenomenon indicated that MnFe-TOS exhibited a good adsorption and oxidation capacity for NO, while the MnFe-TiO₂ showed a strong adsorption ability for SO₂.

In addition, we also investigated the competing adsorption behavior of NO and SO₂ on the catalyst surface at the reaction temperature

200 °C. As shown in Fig. 9C, bridging nitrate (1624 cm^{-1}), nitrites (1429 cm^{-1}), $\text{N}_2\text{O}_2^{\cdot}$ (1360 cm^{-1}), bidentate nitrate (1278 cm^{-1}), and bridging nitrite (1200 cm^{-1}) could still be clearly detected on MnFe-TOS. However, as depicted in Fig. 9D, the NO adsorption was severely inhibited on the MnFe-TiO₂ while its active sites were occupied by $\text{SO}_4^{\cdot 2-}$ (1245 cm^{-1}) [8]. This confirmed that SO_2 does not affect the adsorption and oxidation of NO on the surface of MnFe-TOS, while MnFe-TiO₂ is very sensitive to SO_2 making the NO adsorption and oxidation behavior severely limited.

4.2. Transient reaction process

To reveal the reaction pathway, transient reaction of $\text{NO} + \text{SO}_2 + \text{O}_2$ with preabsorbed NH_3 was conducted over the MnFe-TOS and MnFe-TiO₂ at 200 °C, corresponding in situ DRIFTS spectra were illustrated in Fig. 10A and B. Taking MnFe-TOS for an example (Fig. 10A-A1), once exposed to $\text{NO} + \text{SO}_2 + \text{O}_2$ flow, all bands of pre-adsorbed NH_3 , especially the- NH_2 species at 1326 cm^{-1} and NH_3 coordinately linked to Lewis acid sites at 1597 cm^{-1} , became weakening. Three minutes later, a band due to $(\text{NH}_4)_2\text{SO}_4$ emerged at 1435 cm^{-1} . After 10 min, the band at 1435 cm^{-1} was consumed, and other bands identical to the previous $\text{NO} + \text{SO}_2 + \text{O}_2$ adsorption (Fig. 9C) began to appear and enhanced. Above results implied that $(\text{NH}_4)_2\text{SO}_4$ is readily disassembled into NH_4^+ and $\text{SO}_4^{\cdot 2-}$ on the MnFe-TOS, where NH_4^+ is involved in the SCR reaction as a key transition state. In summary, as important reactive species, - NH_2 species and NH_3 coordinately linked to Lewis acid sites as well as NH_4^+ bonded to Brønsted acid sites on the MnFe-TOS could quickly reacted with gas NO followed E-R pathway [42].

When $\text{NO} + \text{SO}_2 + \text{O}_2$ flow was introduced to MnFe-TiO₂ with pre-adsorbed NH_3 (Fig. 10B-B1), the NH_4^+ on Brønsted acid sites and NH_3 species linked to Lewis acid sites were completely consumed after 7 min, accompanied by emerging of large amounts of monodentate nitrite (1606 cm^{-1}) and bidentate nitrate (1580 cm^{-1}). It was not until 25 min later that the catalyst surface was saturated with adsorption and accumulated some bridging nitrate (1624 cm^{-1}), bidentate nitrate (1517 cm^{-1}), chelating nitrite (1340 cm^{-1}), as well as large amounts of SO_2 (1298 cm^{-1}) and $\text{SO}_4^{\cdot 2-}$ (1245 , 1170 cm^{-1}). Different from the adsorption results of $\text{NO} + \text{SO}_2 + \text{O}_2$ in Fig. 9D, the pre-adsorption of NH_3 on MnFe-TiO₂ promoted its adsorption capacity for NO and SO_2 , which should be interpreted as the enhanced adsorption effect induced by reaction atmosphere [46]. According to literature reports [4,47], the overoxidation of NO to nitrate reacted with ammonia would generate key intermediate NH_2NO and finally lead to the formation of N_2O via nitrate path [12]. This well explained why MnFe-TiO₂ showed poor N_2 selectivity. In totally, important reactive species such as the NH_4^+ on Brønsted acid sites and NH_3 species linked to Lewis acid sites were consumed slowly on MnFe-TiO₂ because of the strong adsorption to SO_2 leaded to large amounts of sulfates covering the active sites. Even worse, the overoxidation of nitrate ammonia resulted in formation of N_2O via nitrate path.

Reverse transient reaction experiments of NH_3 reacted with pre-adsorbed $\text{NO} + \text{SO}_2 + \text{O}_2$ were also performed. As shown in Fig. 10C-C1, bridging nitrate (1624 cm^{-1}), nitrites (1429 cm^{-1}), $\text{N}_2\text{O}_2^{\cdot}$ (1360 cm^{-1}), bidentate nitrate (1278 cm^{-1}), and bridging nitrite (1200 cm^{-1}) on MnFe-TOS were reduced due to the introduction of NH_3 and consumed out after 10 min. Continuous ammonia intake caused excess ammonia finally adsorbed to Lewis acid sites (1597 , 1336 , 1244 , and 1107 cm^{-1}) and Brønsted acid sites (1680 , 1430 cm^{-1}). An interesting phenomenon was that two new peaks appeared at 1370 and 1350 cm^{-1} and soon vanished during 5–7 min, which should be ascribed to the generation and decomposition of $(\text{NH}_4)_2\text{SO}_4$. It confirmed that the $(\text{NH}_4)_2\text{SO}_4$ formed on MnFe-TOS can be easily decomposed into NH_4^+ and $\text{SO}_4^{\cdot 2-}$ while NH_4^+ participating the SCR performance. As a result, the L-H reaction pathway on MnFe-TOS was easily occurring [42].

Since NO adsorption on the MnFe-TiO₂ was severely inhibited because that active sites were occupied by $\text{SO}_4^{\cdot 2-}$, the L-H reaction

pathway on MnFe-TiO₂ was almost blocked and more surface acid sites would generate. Thus, its adsorption capacity for NH_3 would be effectively enhanced. As shown in Fig. 10D-D1, when exposing the MnFe-TiO₂ catalyst with pre-adsorbed $\text{NO} + \text{SO}_2 + \text{O}_2$ into NH_3 atmosphere, large amount of NH_4^+ bonded to Brønsted acid sites (1680 , and 1430 cm^{-1}) and NH_3 coordinately linked to Lewis acid sites (1336 , and 1255 cm^{-1}) were accumulated over time.

4.3. DFT calculations

DFT configurations of MnFe-TOS for further simulating the pre-sulfurization effects on electronic properties were built based on the above characterization analysis. Anatase TiO₂(101) with 144 atoms was selected as slab model. At the beginning, the position of S atom on TiO₂ has been identified. Comparison of S substitution of one surface O atom or Ti atom revealed that the S replaced one surface O atom system S-TiO₂(101) was more energetically stable. As shown in Fig. 3E1–3, S substitution of TiO₂ surface O resulted in surface bulging with an S–O bond length of 1.86 \AA and an S–Ti bond length of 2.37 \AA . This calculation provided reliable evidence for the occurrence of lattice distortion in TiO₂ induced by pre-sulfurization. When MnO₂ was loaded on S-TiO₂(101), Mn of MnO₂ was bonded to S and O bonded to Ti of TiO₂ (Fig. 3F1–2). Immediately after that, we simulated two cases (adjacent and away) of Fe₂O₃ and MnO₂ loaded on S-TiO₂(101), and the comparison in Fig. S10 revealed that the total energy ($E = -1337.11\text{ eV}$) reached the lowest when Fe₂O₃ was closer to MnO₂, indicating that Fe₂O₃ adjacent to MnO₂ loaded on S-TiO₂(101) was the most structurally reasonable. As depicted in Fig. 3G, there is a strong interaction between Fe₂O₃ and MnO₂, forming a Mn–O–Fe–S tetra-atomic ring interface. Above calculations provide compelling evidence demonstrating that pre-implantation of S atom caused TiO₂ lattice distortion and induced interfacial confinement effect favoring the formation of strong interactions between Mn–O–Fe.

Next, we investigated the chemisorption properties of NO, NH_3 , and SO_2 on the catalytic active centers as well as the concomitant charge transfer behavior (Tables S3–4), and corresponding adsorption/total energy of each model system were collected in Table S5. The adsorption sites of NH_3 over MnFe-TOS were first determined in Fig. 8E-G, and found that NH_3 tended to be adsorbed on Fe atoms away from Mn and the adsorption energy ($E_{\text{ads}} = -1.625\text{ eV}$) was the lowest (Fig. 8F1). Bader electron analysis results in Table S3 showed that NH_3 loses electrons (0.282 eV) and N in NH_3 was oxidized. Similarly, the E_{ads} of NO on MnFe-TOS was also measured on different adsorption sites shown in Fig. S11, it could be found that the adsorption energy ($E_{\text{ads}} = -2.85\text{ eV}$) of the system was most stable with NO adsorbed on Fe atom at the interface adjacent to Mn sites with N atom (Fig. 9E1), where NO obtained 0.24 eV electrons since S-TiO₂, MnO₂, and Fe₂O₃ all lost electrons (Table S4). Importantly, the SO_2 adsorption sites over the MnFe-TOS were also simulated in Fig. S12. The optimized results showed that SO_2 did not tend to adsorb on the Mn–O–Fe–S tetra-atomic active center, preferring to adsorb on Fe atoms at the interface (Fig. 9F1, where $E_{\text{ads}} = -0.125\text{ eV}$, or not (Fig. 9G1, where $E_{\text{ads}} = -0.57\text{ eV}$). That is, the adsorption of SO_2 is much suppressed on the MnFe-TOS as a result of enhanced acidity and strong interaction between Mn–O–Fe by pre-sulfurization. To verify the in-situ DRIFTS results of $(\text{NH}_4)_2\text{SO}_4$ decomposition in Fig. 10A-A1, DFT calculations were further applied to explore the adsorption sites of NH_4^+ and $\text{SO}_4^{\cdot 2-}$ on MnFe-TOS catalyst. As shown in Fig. 10E-F, $\text{SO}_4^{\cdot 2-}$ tended to be adsorbed onto the Fe sites, while NH_4^+ was directly involved in the reaction.

Overall, these calculations provide convincing evidence at the molecular level to demonstrate how pre-sulfurization affected the chemical adsorption characteristics of catalytic active centers. Combining the results of in situ DRIFTS experiments and DFT calculations, the reaction schematic on the conventional MnFe-TiO₂ catalyst and the pre-sulfurization-induced interfacial confined MnFe-TOS catalyst was compared in Scheme 1. We concluded that a small amount of S atoms

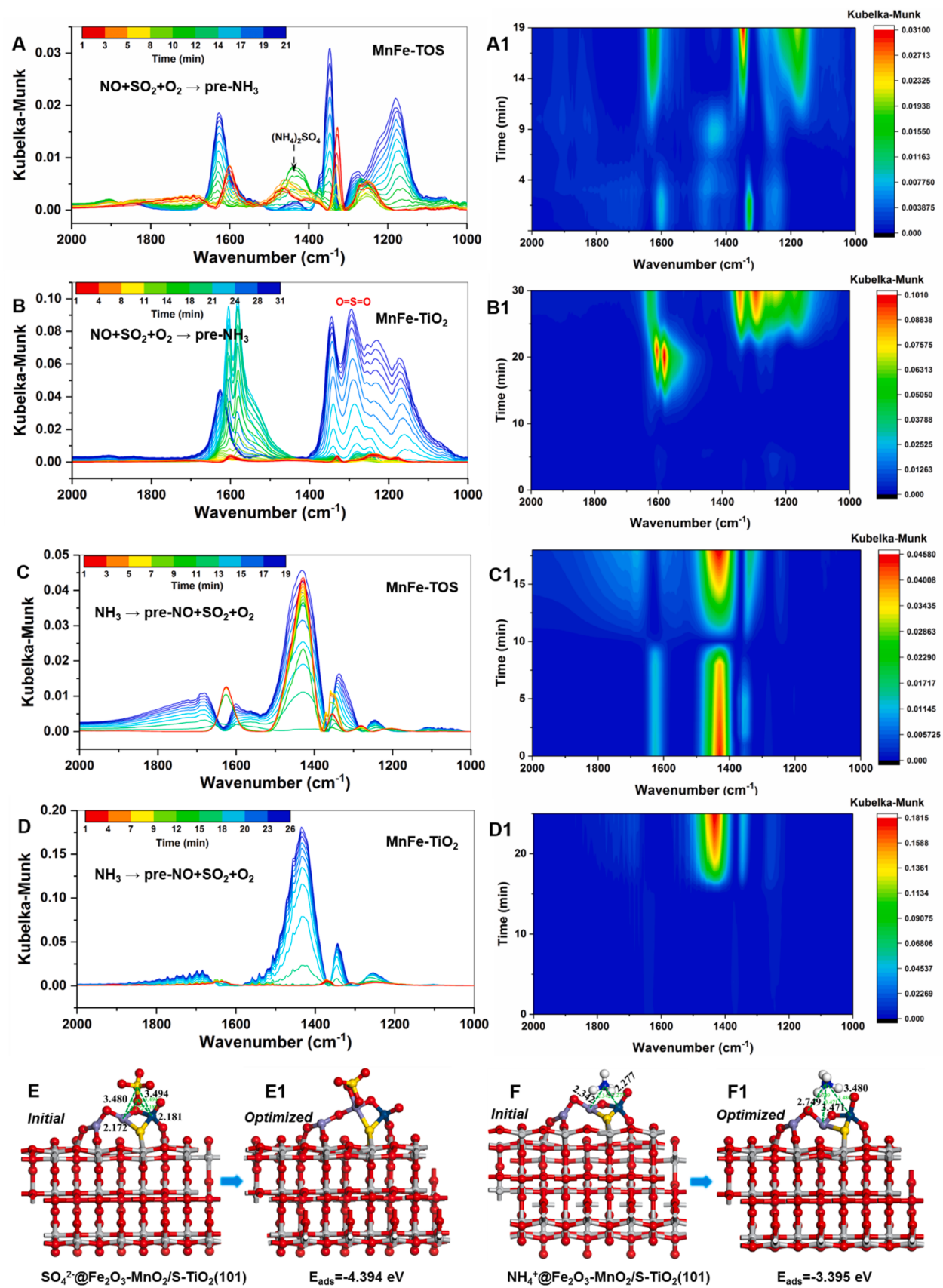
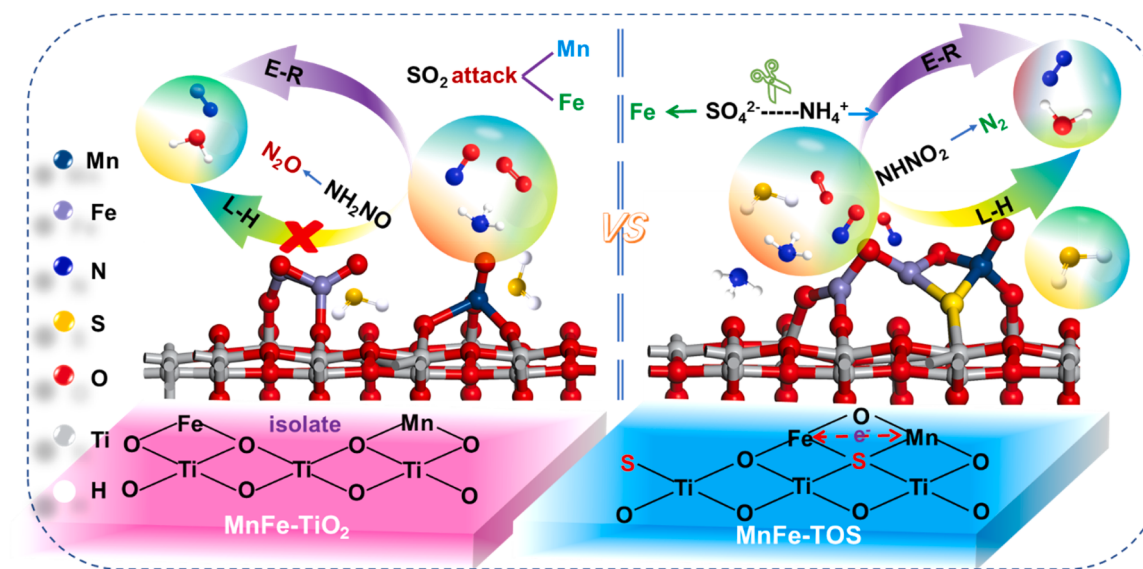


Fig. 10. In-situ DRIFTS of $\text{NO} + \text{SO}_2 + \text{O}_2$ reacted with pre-adsorbed NH_3 (A-A1, B-B1) and NH_3 reacted with pre-adsorbed $\text{NO} + \text{SO}_2 + \text{O}_2$ (C-C1, D-D1) on MnFe-TOS and MnFe-TiO₂ at 200 °C. The adsorption model and adsorption energy on MnFe-TOS of SO_4^{2-} (E, E1), and NH_4^+ (F, F1), red ball: O, gray ball: Ti, yellow ball: S, cyan ball: Mn, purple ball: Fe, white ball: H, and blue ball: N.



Scheme 1. Schematic diagram of reaction mechanism.

replace some O atoms caused lattice distortion of TiO_2 and induced interfacial confinement effect, forming a Mn–O–Fe–S tetra-atomic ring interface on the MnFe-TOS surface. This strong interaction promoted the electron transfer of active centers and effectively inhibited the adsorption of SO_2 at the active site. During the reaction process, the SO_4^{2-} ions generated by the dissociation of $(\text{NH}_4)_2\text{SO}_4$ tend to adsorb on the Fe site, thereby protecting the Mn site from affecting the electron cycle during the reaction process. Therefore, the catalyst exhibited good catalytic activity and resistance to SO_2 poisoning.

5. Conclusion

In this work, pre-sulfurization of the MnFe-TOS catalyst for NH_3 -SCR was skillfully achieved through simple hydrolysis of TiOSO_4 . The insertion of SO_4^{2-} into the TOS carrier not only caused TiO_2 lattice distortion and induced interfacial confinement effects to form strong Mn–O–Fe interactions; but also perturbed the local electronic environment to supplement rich surface acid sites, promoting the rapid adsorption of NH_3 at reaction temperature. Active ammonia species, such as $-\text{NH}_2$ on Lewis acid sites and NH_4^+ on Brønsted acid sites, could be quickly consumed by NO/nitrates via both E-R and L-H reaction pathway and resulted in high N_2 selectivity. Importantly, strong interaction between Mn and Fe adjusted MnFe-TOS redox ability, where the adsorption/activation of NO easily occurred since SO_2 adsorption/oxidation has been effectively suppressed, and DFT calculations also confirmed that SO_2 did not tend to be adsorbed on the Mn–O–Fe–S active center in MnFe-TOS. Furthermore, the $(\text{NH}_4)_2\text{SO}_4$ generated on MnFe-TOS was easily dissociated into NH_4^+ and participated in the SCR reaction. Fe could also serve as a functional protective site to preferentially contact SO_4^{2-} to form $\text{Fe}_2(\text{SO}_4)_3$, protecting Mn sites from attack. Thus, MnFe-TOS demonstrated excellent tolerance to SO_2 . For ordinary MnFe-TiO₂ catalyst, although its low-temperature activity was good, isolated Mn sites were easily attacked by SO_2 to form manganese sulfates. The competitive adsorption of SO_2 seriously inhibited the adsorption and activation of NO, blocking the L-H reaction pathway. The enhanced adsorption effect induced by reaction atmosphere caused NO peroxidation and delayed the E-R reaction pathway with generating a large amount of N_2O through the nitrate pathway, resulting in poor N_2 selectivity. This study provided a new approach for the design of low-temperature NH_3 -SCR catalyst that improve N_2 selectivity and tolerance to SO_2 poisoning.

CRediT authorship contribution statement

Xiaosheng Huang and Ningjie Fang contributed equally to this work: Investigation, Methodology, Formal analysis, DFT calculation, Writing original draft. Shilin Wu: Computational modeling, Data curation. Fang Dong: Conceptualization, Writing – review & editing. Yinghao Chu: Supervision, Resources. Zhicheng Tang: Supervision, Funding acquisition.

Declaration of Competing Interest

The authors declare that they have no known competing financial interests or personal relationships that could have appeared to influence the work reported in this paper.

Data Availability

The authors do not have permission to share data.

Acknowledgments

This work was supported by the National Natural Science Foundation of China (22206189), the Natural Science Foundation of Shandong Province (ZR2023QE116), the Natural Science Foundation of Gansu Province (23JRRA620), the Science and Technology Planning Project of Chengguan District of Lanzhou City (2022-6-2), the Key talent project of Gansu Province, Lanzhou Talent Innovation and Entrepreneurship Project (2022-RC-10), and Major Program of the Lanzhou Institute of Chemical Physics, CAS (No. ZYFZFX-10).

Appendix A. Supporting information

Supplementary data associated with this article can be found in the online version at doi:10.1016/j.apcatb.2023.123518.

References

- [1] M. Li, M. Gao, G. He, Y. Yu, H. He, Mechanistic insight into the promotion of the low-temperature NH_3 -selective catalytic reduction activity over $\text{Mn}_x\text{Ce}_{1-x}\text{O}_y$ catalysts: a combined experimental and density functional theory study, Environ. Sci. Technol. 57 (2023) 3875–3882.
- [2] W. Qu, X. Liu, J. Chen, Y. Dong, X. Tang, Y. Chen, Single-atom catalysts reveal the dinuclear characteristic of active sites in NO selective reduction with NH_3 , Nat. Commun. 11 (2020) 1532.

- [3] D. Wang, Q. Chen, X. Zhang, C. Gao, B. Wang, X. Huang, Y. Peng, J. Li, C. Lu, J. Crittenden, Multipollutant Control (MPC) of flue gas from stationary sources using SCR technology: a critical review, *Environ. Sci. Technol.* 55 (2021) 2743–2766.
- [4] Y. Che, X. Liu, Z. Shen, K. Zhang, X. Hu, A. Chen, D. Zhang, Improved N₂ selectivity of MnO_x catalysts for NO_x reduction by engineering bridged Mn³⁺ Sites, *Langmuir* 39 (2023) 7434–7443.
- [5] W. Qu, H. Yuan, Z. Ren, J. Qi, D. Xu, J. Chen, L. Chen, H. Yang, Z. Ma, X. Liu, H. Wang, X. Tang, An atom-pair design strategy for optimizing the synergistic electron effects of catalytic sites in NO selective reduction, *Angew. Chem. Int. Ed. Engl.* 61 (2022), e202212703.
- [6] K. Guo, J. Ji, W. Song, J. Sun, C. Tang, L. Dong, Conquering ammonium bisulfate poison over low-temperature NH₃-SCR catalysts: A critical review, *Appl. Catal. B* 297 (2021), 120388.
- [7] J. Ji, N. Gao, W. Song, Y. Tang, Y. Cai, L. Han, L. Cheng, J. Sun, S. Ma, Y. Chu, C. Tang, L. Dong, Understanding the temperature-dependent H₂O promotion effect on SO₂ resistance of MnO_x-CeO₂ catalyst for SCR denitrification, *Appl. Catal. B* 324 (2023), 122263.
- [8] S. Li, L. Song, J. Li, H. He, Promotional mechanisms of activity and SO₂ tolerance of NdVO_x/TiO₂ catalysts for selective catalytic reduction of NO_x with NH₃, *ACS Catal.* 13 (2023) 2867–2884.
- [9] L. Han, S. Cai, M. Gao, J.Y. Hasegawa, P. Wang, J. Zhang, L. Shi, D. Zhang, Selective catalytic reduction of NO_x with NH₃ by using novel catalysts: state of the art and future prospects, *Chem. Rev.* 119 (2019) 10916–10976.
- [10] L. Yan, Y. Gu, L. Han, P. Wang, H. Li, T. Yan, S. Kuboon, L. Shi, D. Zhang, Dual promotional effects of TiO₂-decorated acid-treated MnO_x octahedral molecular sieve catalysts for alkali-resistant reduction of NO_x, *ACS Appl. Mater. Interfaces* 11 (2019) 11507–11517.
- [11] J. Tang, X. Wang, H. Li, L. Xing, M. Liu, The resistance of SO₂ and H₂O of Mn-based catalysts for NO_x selective catalytic reduction with ammonia: recent advances and perspectives, *ACS Omega* 8 (2023) 7262–7278.
- [12] S. Yang, S. Xiong, Y. Liao, X. Xiao, F. Qi, Y. Peng, Y. Fu, W. Shan, J. Li, Mechanism of N₂O formation during the low-temperature selective catalytic reduction of NO with NH₃ over Mn-Fe spinel, *Environ. Sci. Technol.* 48 (2014) 10354–10362.
- [13] Y. Wang, L. Chen, W. Wang, X. Wang, B. Li, S. Zhang, W. Li, S. Li, Revealing the excellent low-temperature activity of the Fe_{1-x}Ce_xO₃-S Catalyst for NH₃-SCR: improvement of the lattice oxygen mobility, *ACS Appl. Mater. Interfaces* 15 (2023) 17834–17847.
- [14] F. Wang, Z. Xie, J. Liang, B. Fang, Y. Piao, M. Hao, Z. Wang, Tourmaline-modified FeMnTiO_x catalysts for improved low-temperature NH₃-SCR performance, *Environ. Sci. Technol.* 53 (2019) 6989–6996.
- [15] K. Song, K. Guo, Y. Lv, D. Ma, Y. Cheng, J.W. Shi, Rational regulation of reducibility and acid site on Mn-Fe-BTC to achieve high low-temperature catalytic denitrification performance, *ACS Appl. Mater. Interfaces* 15 (2023) 4132–4143.
- [16] X. Huang, F. Dong, G. Zhang, Y. Guo, Z. Tang, A strategy for constructing highly efficient yolk-shell Ce@Mn/TiO₂ catalyst with dual active sites for low-temperature selective catalytic reduction of NO with NH₃, *Chem. Eng. J.* 419 (2021), 129572.
- [17] C. Gao, B. Xiao, J.-W. Shi, C. He, B. Wang, D. Ma, Y. Cheng, C. Niu, Comprehensive understanding the promoting effect of Dy-doping on MnFeO_x nanowires for the low-temperature NH₃-SCR of NO_x: An experimental and theoretical study, *J. Catal.* 380 (2019) 55–67.
- [18] C. Huang, R. Guo, W. Pan, X. Sun, S. Liu, J. Liu, Z. Wang, X. Shi, SCR of NO_x by NH₃ over MnFeO_x@TiO₂ catalyst with a core-shell structure: the improved K resistance, *J. Energy Inst.* 92 (2019) 1364–1378.
- [19] Z. Cai, G. Zhang, Z. Tang, J. Zhang, MnFeO_x@TiO₂ nanocages for selective catalytic reduction of NO with NH₃ at low temperature, *ACS Appl. Nano Mater.* 4 (2021) 6201–6211.
- [20] Z. Cai, G. Zhang, Z. Tang, J. Zhang, MnFe@CeO_x core–shell nanocages for the selective catalytic reduction of NO with NH₃ at low temperature, *ACS Appl. Nano Mater.* 5 (2022) 3619–3631.
- [21] Q. Xie, Y. Cai, L. Zhang, Z. Hu, T. Li, X. Wang, Q. Zeng, X. Wang, J. Sun, L. Dong, Relationships between adsorption amount of surface sulfate and NH₃-SCR performance over CeO₂, *J. Phys. Chem. C.* 125 (2021) 21964–21974.
- [22] H. Liu, S. Xiong, H. Ou, H. Lei, J. Li, L. He, J. Li, The contradictory impact of sulfation on a CeO_x/TiO₂ NH₃-SCR catalyst: a combined experimental and DFT study, *Energy Fuels* 37 (2023) 6674–6682.
- [23] Z. Chen, R.-t Guo, S. Ren, L. Chen, X. Li, M. Wang, Comparative analysis of the dual origins of the N₂O byproduct on MnO_x, FeO_x, and MnFeO_x sphere catalysts for a low-temperature SCR of NO with NH₃, *J. Mater. Chem. A* 10 (2022) 21474–21491.
- [24] K.H. Hwang, N. Park, H. Lee, K.-M. Lee, S.W. Jeon, H.S. Kim, Y. Lee, T.J. Kim, W. B. Lee, D.H. Kim, Mechanochemical localization of vanadia on titania to prepare a highly sulfur-resistant catalyst for low-temperature NH₃-SCR, *Appl. Catal. B* 324 (2023), 122290.
- [25] G. Zhang, W. Han, H. Zhao, L. Zong, Z. Tang, Solvothermal synthesis of well-designed ceria-tin-titanium catalysts with enhanced catalytic performance for wide temperature NH₃-SCR reaction, *Appl. Catal. B* 226 (2018) 117–126.
- [26] X. Huang, F. Dong, G. Zhang, Z. Tang, Modification of composite catalytic material CumVnOx@CeO₂ core–shell nanorods with tungsten for NH₃-SCR, *Nanoscale* 12 (2020) 16366–16380.
- [27] C. Wang, F. Gao, S. Ko, H. Liu, H. Yi, X. Tang, Structural control for inhibiting SO₂ adsorption in porous MnCe nanowire aerogel catalysts for low-temperature NH₃-SCR, *Chem. Eng. J.* 434 (2022), 134729.
- [28] D. Shu, T. Chen, H. Liu, H. Xie, X. Zou, P. Zhang, C. Wang, Z. Han, D. Chen, A novel superior Fe-Ce-V catalyst with high performance for selective catalytic reduction of NO_x with NH₃, *Appl. Surf. Sci.* 608 (2023), 154978.
- [29] K. Song, K. Guo, S. Mao, D. Ma, Y. Lv, C. He, H. Wang, Y. Cheng, J.-W. Shi, Insight into the origin of excellent SO₂ tolerance and de-NO_x performance of quasi-Mn-BTC in the low-temperature catalytic reduction of nitrogen oxide, *ACS Catal.* 13 (2023) 5020–5032.
- [30] R. Yin, J. Chen, L. Shan, J. Shi, K. Yang, H. Liu, J. Li, Prominent difference in the deactivation rate and mechanism of V₂O₅/TiO₂ under H₂S or SO₂ during selective catalytic reduction of NO_x with NH₃, *Appl. Catal. B* 328 (2023), 122529.
- [31] D. Fang, K. Qi, F. Li, F. He, J. Xie, Excellent sulfur tolerance performance over Fe-SO₄/TiO₂ catalysts for NH₃-SCR: Influence of sulfation and Fe-based sulfates, *J. Environ. Chem. Eng.* 10 (2022), 107038.
- [32] C. Feng, L. Han, P. Wang, X. Liu, G. Zhou, D. Zhang, Unraveling SO₂-tolerant mechanism over Fe₂(SO₄)₃/TiO₂ catalysts for NO_x reduction, *J. Environ. Sci. (China)* 111 (2022) 340–350.
- [33] Q. Xu, Z. Li, L. Wang, W. Zhan, Y. Guo, Y. Guo, Understanding the role of redox properties and NO adsorption over MnFeO_x for NH₃-SCR, *Catal. Sci. Technol.* 12 (2022) 2030–2041.
- [34] J. Jia, R. Ran, X. Guo, X. Wu, W. Chen, D. Weng, Enhanced low-temperature NO oxidation by iron-modified MnO₂ catalysts, *Catal. Commun.* 119 (2019) 139–143.
- [35] X. Huang, F. Dong, G. Zhang, Z. Tang, Constructing TiO₂@CeMnO_x nanocages by self-sacrificial hydrolytic etching MIL-125 for efficient wide-temperature selective catalytic reduction of nitrogen oxides, *Chem. Eng. J.* 432 (2021), 134236.
- [36] J. Ji, L. Han, W. Song, J. Sun, W. Zou, C. Tang, L. Dong, Promotion effect of bulk sulfates over CeO₂ for selective catalytic reduction of NO by NH₃ at high temperatures, *Chin. Chem. Lett.* 34 (2023), 107769.
- [37] D. An, S. Yang, W. Zou, J. Sun, W. Tan, J. Ji, Q. Tong, C. Sun, D. Li, L. Dong, Unraveling the SO₂ poisoning effect over the lifetime of MeO_x (Me = Ce, Fe, Mn) catalysts in low-temperature NH₃-SCR: interaction of reaction atmosphere with surface species, *J. Phys. Chem. C.* 126 (2022) 12168–12177.
- [38] Z. Lian, W. Shan, M. Wang, H. He, Q. Feng, The balance of acidity and redox capability over modified CeO₂ catalyst for the selective catalytic reduction of NO with NH₃, *J. Environ. Sci. (China)* 79 (2019) 273–279.
- [39] H. Liu, C. Gao, J. Chen, J. Mi, S. Yang, D. Chen, W. Si, Y. Peng, C. Sun, J. Li, Optimized local geometry and electronic structure of MoO₃/CeO₂ catalyst by adding copper cations for boosted nitrogen oxide reduction performance, *Appl. Catal. B* 332 (2023), 122742.
- [40] D. Meng, Q. Xu, Y. Jiao, Y. Guo, L. Wang, G. Lu, W. Zhan, Spinel structured CoAlMnO_x mixed oxide catalyst for the selective catalytic reduction of NO_x with NH₃, *Appl. Catal. B* 221 (2018) 652–663.
- [41] X. Yao, K. Kang, J. Cao, L. Chen, W. Luo, W. Zhao, J. Rong, Y. Chen, Enhancing the denitration performance and anti-K poisoning ability of CeO₂-TiO₂/P25 catalyst by H₂SO₄ pretreatment: Structure-activity relationship and mechanism study, *Appl. Catal. B* 269 (2020), 118808.
- [42] W. Chen, R. Zou, X. Wang, Toward an atomic-level understanding of the catalytic mechanism of selective catalytic reduction of NO_x with NH₃, *ACS Catal.* 12 (2022) 14347–14375.
- [43] L.-Y. Lin, T.-T. Hsieh, J.-C. Hsu, Y.-C. Wang, Insight into the enhanced catalytic activity and H₂O/SO₂ resistance of MnFeO_x/defect-engineered TiO₂ for low-temperature selective catalytic reduction of NO with NH₃, *Appl. Surf. Sci.* 614 (2023), 156139.
- [44] X. Huang, F. Dong, G. Zhang, Z. Tang, Design and identify the confinement effect of active site position on catalytic performance for selective catalytic reduction of NO with NH₃ at low temperature, *J. Catal.* 420 (2023) 134–150.
- [45] Z. Xu, S. Impeng, X. Jia, F. Wang, Y. Shen, P. Wang, D. Zhang, SO₂-Tolerant catalytic reduction of NO_x by confining active species in TiO₂ nanotubes, *Environ. Sci. Nano* 9 (2022) 2121–2133.
- [46] H. Xin, L. Lin, R. Li, D. Li, T. Song, R. Mu, Q. Fu, X. Bao, Overturning CO(2) hydrogenation selectivity with high activity via reaction-induced strong metal-support interactions, *J. Am. Chem. Soc.* 144 (2022) 4874–4882.
- [47] M. Gao, Z. Li, G. He, Y. Shan, Y. Sun, H. He, Unveiling the origin of selectivity in the selective catalytic reduction of NO with NH₃ over oxide catalysts, *Environ. Sci. Technol.* 57 (2023) 8426–8434.